Molecular Components of Catalytic Selectivity

Gabor A. Somorjai [1, 2,]* and Jeong Y. Park [2]

[1]Department of Chemistry, University of California, Berkeley, CA 94720

[2]Materials Sciences Division and Chemical Sciences Division, Lawrence Berkeley National Laboratory, Berkeley, CA 94720

Abstract

*To whom correspondence should be addressed. E-mail: somorjai@berkeley.edu

Keywords:

Catalytic activity and selectivity

Platinum and rhodium nanoparticle

Multi-path reactions

Reaction intermediates

Adsorbate induced restructuring and adsorbate mobility

From the Contents

1. Introduction

2. Selectivity in Heterogeneous Catalysis

3. Catalysts are Nanoparticles – Evolution of Model Surfaces

4. Colloid Chemistry Controlled Nanoparticle Synthesis

5. Characterization and Catalytic Reactions of Two-Dimensional and Three-Dimensional Metal Nanoparticle Catalyst Systems

6. The Influence of Size and Shape of Nanoparticles on Reaction Selectivity

7. The Role of Capping Layers on Nanoparticles in Catalytic Reaction

8. Seven Molecular Components of Catalytic Selectivity

- **8.a. Surface Structure**
- **8.b. Adsorbate-Induced Restructuring**
- **8.c. Adsorbate Mobility**
- **8.d. Reaction Intermediates**
- **8.e. Surface Composition**
- **8.f. Charge Transport**
- **8.g. Oxidation States**

9. Future Perspective

Abstract

Selectivity, that is, to produce one molecule out of many other thermodynamically feasible product molecules, is the key concept to develop "clean manufacturing" processes that do not produce byproducts (green chemistry). Small differences in potential energy barriers for elementary reaction steps control which reaction channel is more likely to yield the desired product molecule (selectivity), instead of the overall activation energy for the reaction that controls turnover rates (activity). Recent studies have demonstrated the atomic- or molecular-level tailoring of parameters such as the surface structures of active sites that give rise to nanoparticle size and shape dependence of turnover rates and reaction selectivities. Here, we highlight seven molecular components that influence reaction selectivities. These include: surface structure, adsorbate-induced restructuring, adsorbate mobility, reaction intermediates, surface composition, charge transport, and oxidation states for model metal single crystal and colloid nanoparticle catalysts. We show examples of their functioning and describe in-situ instruments that permit us to investigate their roles in surface reactions.

I. Introduction

During the 20th century, catalysis science evolved using model surfaces, developing instrumentation for molecular studies of surface chemistry including the structures, dynamics and chemical bonding of atoms and molecules at surfaces, and simultaneously measuring reaction rates and product selectivities [1-3]. Most of the studies were carried out by using single-product catalytic reactions such as ammonia synthesis, carbon monoxide oxidation or ethylene hydrogenation. Development of new and useful catalysts for carrying out multi-path reactions with high selectivity that leads to major gains in energy efficiency as undesirable byproducts are eliminated are our goal in the 21st century [4]. Decades of research and development have produced industrial catalysts that possess nanosize features which contribute in a fundamental way to their function (activity and selectivity) [3]. For porous materials (e.g., those based on zeolites) [5-7] the pore size can exclude molecules with diameters larger than the pore to approach the active site inside the pore, while smaller molecules can enter and react. For metal catalyst particles, the presence of three-fold sites can facilitate organic rearrangements that produce aromatic molecules and sites of different atomic coordination from atomic steps and kinks to larger ensembles break chemical bonds, H-H, C-H, C-C, C=O, O=O, selectively. Oxide-metal interface sites are implicated in changing both the activity and selectivity of multi-path reactions, such as carbon monoxide hydrogenation[8]. Recent advances in synthetic nanotechnology and *in-situ* techniques revealed correlations between catalyst selectivity and the size and shape of the metal catalyst particles and their location and bonding on the oxide support [9-12].

In this review, we highlight recent findings of molecular-level properties that govern reaction selectivities of transition metals mostly platinum and rhodium at low temperatures, <300 ^{o}C. We describe the challenge of fine-tuning of potential energy barrier heights to control selectivity in heterogeneous catalysis in section 2. In section 3, we emphasize that the three catalyst systems (enzyme, heterogeneous and homogeneous) are nanoparticles. This observation drives the evolution of model catalyst surfaces from studies of single crystals to studies of nanoparticles in the 1-10 nm size range. In section 4, we describe the nanoparticle synthesis controlled by colloid chemistry that appears at present to be the most versatile fabrication for controlling the size and shape of nanoparticles. We show recent results on dendrimer-encapsulated platinum and rhodium nanoparticles that have cluster sizes of one nm or less. In section 5, fabrication and characterization of two-dimensional and three-dimensional nanoparticle systems are described. Then, we give examples of the particle size and shape dependence of catalytic selectivity in section 6, which appear to be major components for developing catalysts with 100% selectivity. We explore why, on a molecular scale, the particle size and shape dependence of nano-catalysts are occurring. In section 7, we discuss the influence of capping layers of colloid nanoparticles on the catalytic activity and selectivity, and how they might be removed or modified. In section 8, we list seven molecular properties that are responsible for the selectivity of catalytic reaction. One example is given for each from surface science studies in Berkeley over the years. These are: surface structure (section 8.1), adsorbate-induced restructuring (section 8.2), adsorbate mobility (section 8.3), reaction intermediates (section 8.4), surface composition (section 8.5), charge transport (section 8.6), and oxidation states (section 8.7). The techniques that provide

molecular information on catalytic surface reactions are introduced with a special emphasis on three instruments, the scanning tunneling microscope (STM) that operates at high pressures [13], the high pressure sum frequency generation (SFG) vibrational spectroscopy instrument [14]and the ambient pressure X-ray photoelectron spectroscopy [15], which have been developed recently in Berkeley and provide oxidation states of the catalyst' surface during catalytic reactions *in-situ*. Finally, in section 9, we argue for the importance of combined studies of enzyme, homogeneously-catalyzed and heterogeneously-catalyzed reactions under the same experimental conditions, and preferably the same reactions in the future.

In this review, a) we emphasizes the need for focus on reaction selectivity, instead of activity, as the next grand challenge of catalysis; b) We show the evolution of the science of nanomaterials has permitted the use of nanoparticles as model systems, which is the natural habitat of catalysis; c) We show evolution of characterization techniques has permitted molecular investigation of the catalyst surface under reaction conditions. We hope this review gives a roadmap for catalysis science using the model system approach. The vertical integration of catalysis research to pursue synthesis, characterization and reaction kinetic studies have accelerated progress in the field.

2. Selectivity in Heterogeneous Catalysis

Product selectivity is essential in developing processes that yield the desired molecules in multi-path reactions with 100% selectivity. We chose organic reactions shown in Figure 1 that are catalyzed by platinum and rhodium at low temperatures (<300

^{o}C) and usually form two different product molecules. In this circumstance, instead of a single potential energy barrier that is reflected by the activation energy for the formation of a product, we have several potential energy barriers with small energy differences[16-19]. This is depicted in Figure 1 in a one dimensional potential energy plot for the competitive formation of two products [1, 17]. What determines the reaction selectivity is this relative energy difference of potential energy barriers. Figure 1 shows that very small changes, such as 2 kcal/mol, between potential energy barriers completely change the product distribution. These changes can be induced by co-adsorbates, small structure changes, or the addition of electron donors or acceptors, which change the binding energies of reaction intermediates or adsorbed reactants or products.

In general, the relative heights of activation energy barriers are dependent on the atomic structure, electronic and chemical properties of catalyst surfaces. Controlling the relative barrier height to change the reaction selectivity requires a good understanding of the roles played by structural, dynamic, and electronic properties of model surfaces, which induce the desired chemical change[20-23] We shall show that the shape and size of nanoparticles can be important components of reaction selectivity because the surface structure is determined by the shape of nanoparticles[9, 24], and the density of steps and kinks or oxidation states (that changes the electronic structures of the surface) are directly correlated with the size of nanoparticles. Not only the catalysts but also the types of reactions (reactants and products molecules), and condition of reactions (temperature, pressure, and reaction time and nature of catalyst support) can affect the pathways during the multi-path catalytic reactions which alters reaction Intermediates and surface

mobilities. At the molecular level, we shall outline later in this review seven key factors that influence the relative heights of activation energy barriers, thus, to tune reaction selectivity.

3. Catalysts are Nanoparticles – Evolution of Model Surfaces

While single crystals are used as model surfaces for studies of metal catalysis for decades [1, 16, 25], it should be recognized that all catalysts are nanoparticles, not just metal heterogeneous catalysts, but enzymes and homogeneous catalysts, as well. Examples of these are shown in Figure 2. Cytochrome C, which is one of the over 3000 enzymes that functions in the human body (Figure 2a), is 4 nm in size with its protein shell wrapped around it. The size of its active site (heme) in the enzymatic process is 1.4 nm [26]. A typical homogeneous catalyst used for olefin polymerization is a so-called single-site catalyst with an active site that is a titanium ion surrounded by ligands (Figure 2b), which is 1.6 nm in size [27]. The heterogeneous catalysts, such as platinum or rhodium nanoparticles, are between 1-10 nm in size. In Figure 2c, we show a SEM image of 8 nm $Pt_{0.5}Rh_{0.5}$ bimetallic nanoparticle arrays deposited on silicon wafer with Langmuir-Blodgett technique [28]. We must explore and understand how nanoparticles function in their roles as catalysts as they are used in nature and in the chemical technologies.

With the rise of nanoscience and nanomaterial synthesis, it has become possible to fabricate metal nanoparticles in the 1-10 nm regime, which is identical to the sizes of heterogeneous metal catalysts used as the industrial catalysts. As a result, model studies could be extended from single crystal metal surfaces to nanoparticles of controlled shape

and size. This trend is also related to the issue of "bridging the materials gap" [29, 30]. Single-crystalline metals used for modeling industrial catalysis inherently lack the complexity needed to uncover many of the factors important to catalytic turnover and selectivity. Considerations such as metal support interactions and the importance of metallic cluster size are of extreme importance to catalytic applications. To overcome this problem, several new model systems have been proposed and utilized, as shown in Figure 3.

There is a great deal of experimental evidence indicating that the interface between the metal nanoparticle and the oxide support is an important catalytic site. Since heterogeneous metal catalysts are usually nanoparticles that are deposited on oxide supports, oxide-metal interface are major components of every catalysts systems. Evidences have been accumulated since the early studies by Schwab and his coworkers [31, 32] that the oxide-metal interfaces are responsible for the increase of activity and change of selectivity for many chemical processes. This phenomena has been exploited in the design of the "strong metal-support interaction (SMSI)" catalyst systems in the chemical technologies [8, 33].

Pt nanoparticle and nanowires have been fabricated on oxide surfaces (such as oxidized silicon wafer) using lithography techniques. Pt nanoparticle arrays 50 nm in size were fabricated with electron beam lithography, which utilizes high-resolution pattern writing and an electron-sensitive resist/etching[34-37]. It was found that when the metal was poisoned by adsorbed CO that inhibited catalyst, the turnover rate of ethylene hydrogenation was proportional to the oxide–metal periphery area, suggesting the oxide-metal interface functions as a reactive site[36]. There is another phenomena, hot electron

generation at oxide-metal interfaces during exothermic catalytic reactions that occur during catalytic turnover that is an important property of these interfaces. The resulting flow of charge occurs at the Schottky barrier that is formed at certain oxide-metal interfaces has chemical consequences[38-41]. This will be described in more detail in Section 8f as we believe this charge flow is one of the important molecular components of heterogeneous catalysis which influences reaction selectivity.

4. Colloid Chemistry Controlled Nanoparticle Synthesis

Our focus was on platinum and rhodium nanoparticles and bimetallic nanoparticles with mono-dispersity and well-controlled shape. Using hexachloro platinic acid or rhodium acetyl-acetonate as precursor monomers, monodispersed metal nanoparticles can be produced, each one coated with a polymer cap that prevents aggregation in solution, as shown in Figure 4 [11, 42, 43]. One can show that under well-defined conditions, the particle size is proportional to the monomer concentration and can be controlled by changing the monomer concentration. By tuning the reduction processes, it was possible to control the size and shapes of Pt or Rh nanoparticles [44-47]. Figure 5 shows Pt nanoparticles with controlled shape and size. High resolution transmission electron microscopy (HRTEM) along with electron diffraction analysis reveals the shape of nanoparticles [44]. These mono-dispersed nanoparticles with uniform size and shape can be deposited as a two-dimensional film by using the Langmuir-Blodgett technique. The nanoparticles can also be deposited in a mesoporous, three-dimensional oxide

framework at much higher surface concentrations[48]. Studies of nanoparticles in these different configurations give us model surfaces that overlap the size and morphology of nanoparticles presently used in chemical technology [49].

Recently, small clusters of dendrimer encapsulated metal nanoparticles are being explored for catalysis [50 , 51 , 52 , 53]. Structure and chemical properties of dendrimers, a quasispherical hyperbranched polymer, can be controlled by changing the core structure, the number and type of the duplicating units, and the terminal functional groups, as shown in Figure 6. Poly(amidoamine) (PAMAM) are the most popular ones used in the synthesis of metal nanoparticles. Platinum nanoparticles ranging from less than 1 nm to 4 or 5 nm, have been synthesized within the cavities of high generation PAMAM dendrimers (more than 3rd generation) [54]. The size distribution of metal nanoparticles synthesized within dendrimers is very narrow due to the well-defined composition and structure of the dendrimer template. Recently, we have successfully synthesized monodisperse platinum nanoparticles, with a diameter of 1.6 $\pm$ 0.3 nm, encapsulated within 4th generation PAMAM dendrimers [55].

5. Characterization and Catalytic Reactions of Two-Dimensional and Three-Dimensional Metal Nanoparticle Catalyst Systems

Once nanoparticles are synthesized, they can be placed on a Langmuir-Blodgett trough and pulled as a monolayer film at various densities [49]. This approach allows us to form the two dimensional Pt nanoparticle arrays, as shown in Figure 7a. The average inter-particle spacing can be tuned by varying surface pressure. This approach has the

advantage of controlling the size and composition of the nanoparticles synthesized via this colloidal route and the formation of an oxide–metal interface between the nanoparticles and the substrate. The particles are capped with an organic surfactant or a polymer, which prevents aggregation under solution synthesis conditions. A variety of organic coatings has been used which include TTAB (Tetradecyltrimethylammonium Bromide), hexadecylamine (HDA), hexadecylthiol (HDT), and PVP (poly(vinylpyrrolidone)). Figure 7a shows a TEM image of TTAB capped Pt nanoparticle arrays on a silicon oxide grid.

Conversely, they can be incorporated in mezoporous, high surface area oxides, such as SBA-15 [7, 56] or mesocellulous silica foams (MCF)-1 [57], by sonication or by synthesizing the mesoporous channels around the nanoparticles in the same solution. A TEM image of Pt platinum nanoparticles encapsulated in mesoporous silica with a channel structure (SBA-15) is shown in Figure 7b, as well. This forms a 3D model nanoparticle catalyst system with higher surface area (> 1 m^2/g).

For characterization of chemical, physical and electronic properties of nanoparticles, we have utilized many techniques. Infrared and Fourier transform infrared spectroscopies, Raman spectroscopy, Auger spectroscopy, X-ray photoelectron spectroscopy, small angle X-ray scattering and X-ray diffraction, physisorption and chemisorption are techniques that provide the toolbox for studying two-dimensional or three-dimensional nanoparticles, as listed in Table 1.

Two types of reactors have been used for catalytic turnover studies. The activity and selectivity of monolayer nanoparticle films were studied by a batch reactor, equipped with a recirculation pump, similar to that used for single crystal metal reactivity studies.

The schematic of this catalytic reactor is shown in Figure 8a. Active metal nanoparticles are supported on planar support such as a silicon wafer where they are deposited by Langmuir-Blodgett techniques. The typical metal surface sites available for catalysis on 2D system are 10^{14} to 10^{15}. The schematic of a three-dimensional catalysis system is shown in Figure 8b, where the reaction is performed in differential reactors. Active metal nanoparticles are supported on mesoporous oxides where they are deposited by capillary inclusion or during hydrothermal growth of the oxide. The typical metal reaction sites available for catalysis is 10^{16} to 10^{18}.

6. The Influence of Size and Shape of Nanoparticles on Reaction Selectivity

In this section, we provide several examples how the size and shape of nanoparticles influence reaction selectivities. Typical multi-path reactions utilized to study the reaction selectivity at the molecular level are shown in Scheme 1.

Figure 9 shows the particle size dependence on reaction selectivity for cyclohexene hydrogenation/dehydrogenation and crotonaldehyde hydrogenation [49]. The selectivity of benzene decreases as the size of nanoparticles increases. The reason for this is that the activation energy for dehydrogenation of cyclohexene to benzene increases with increasing particle size, while the activation energy for hydrogenation to cyclohexane is constant and remains unchanged as particle size increases, resulting in declining benzene concentrations.

We studied the nanoparticle size selectivity for multi-path reactions for benzene hydrogenation that produces two molecules [58] (cyclohexane (C_6H_{12}) and cyclohexene

(C_6H_{10})) on the platinum (111) surface and only one molecule (cyclohexene, C_6H_{10}) on the (100) face. What we find is that platinum nanoparticle catalysts, when they are shaped as cuboctahedra, give rise to two products, C_6H_{12} and C_6H_{10}, just like (111) single crystal surfaces, but when they are cubes, they give rise to one product, C_6H_{10}, like the (100) single crystal surface, as shown in Figure 10 [24]. This result indicates that the single crystal studies and the nanoparticle studies show the same surface structure dependence and shape selectivity, indicating that the two types of surfaces are behaving similarly in spite of the difference in size.

Using dendrimers as supports for the nanoparticles, 1 nm or smaller nanoparticles could be produced[55]. The dendrimer cavities stop the growth of nanoparticles at around 1 nm and, this way, we could explore the catalytic activity of small clusters of metals such as rhodium or platinum cluster sizes of 20-30 atoms, as shown in Figure 6. Figure 11 shows how the particle size dependence in this small particle size range is much more dominant than the particle size dependence with larger size nanoparticles for the hydrogenation of pyrrole to pyrrolidine and n-butylamine.

7. The Role of Capping Layers on Nanoparticles in Catalytic Reaction

There are several organic capping materials that have been used. Our general findings indicate that these capping layers do not impede the catalytic reactions significantly due to porous nature of organic capping. On the molecular scale, the porous organic capping layers have open space that permits the reactant and product molecules to pass through the capping layers. We carried out CO oxidation on several platinum

nanoparticle systems capped with various organic molecules to investigate the role of the capping agent on the catalytic activity. In this study, platinum colloid nanoparticles with four types of capping layer have been used; TTAB, HAD, HDT, and PVP [59]. There is a small effect of the presence of the different organic coating on the platinum nanoparticle during CO oxidation. The order of 30 % variation in reaction turnover rates are observed as shown in Figure 12.

However, we can remove the organic caps after depositing the nanoparticles, either in a two-dimensional or a three-dimensional mode by using ultraviolet (UV)-ozone techniques [60]. Figure 13 shows the preliminary results of the sum frequency generation vibrational spectrum of the nanoparticles with the organic caps, then the organic cap removal by the disappearance of the CH-CH_2 stretches due to the organic capping. The adsorption of benzene on the platinum nanoparticle surfaces after UV-ozone technique is revealed by the SFG vibrational spectrum of adsorbed benzene [61].

8. Seven Molecular Components of Catalytic Selectivity

As shown earlier, reaction selectivity is determined by the relative energy difference of potential energy barriers. From the viewpoints of reaction kinetics, selectivity requires control of activation energies within a small fraction of their absolute value. However, the chemical and thermal stabilities of catalysts depend on the reaction condition (temperature, pressure, reaction time and the types of product and reactant molecules, as indicated in Scheme 2. At present we deliberately focus on catalytic reaction selectivity studies at lower temperature, below 600 K, that are less influencing of

the stability of catalyst materials. There are seven molecular level components of selectivity that we can determine from studies so far, as depicted in Scheme 2. These are 1) surface structure, 2) adsorbate-induced restructuring, 3) adsorbate mobility, 4) reaction intermediates, 5) surface composition, 6) charge transport during catalysis and 7) oxidation state of the catalyst. We shall give one example for each.

8.a. Surface Structure

For the study of surface structure, a high pressure-ultra high vacuum combined system was developed (Figure 14a) [30]. This hybrid system permitted both reaction studies at high pressures and surface analysis, which needed vacuum before and after reactions.

The reforming reaction where this multi-path reaction scheme is important produces high-octane gasoline of aromatics and brenched isomers from n-hexene and n-heptane with near zero octane number. Platinum single crystal surface studies indicate that the hexagonal (111) surface produces benzene as a dominant reaction in n-hexene conversion, while the (100) faces prefer to catalyze isomerization reactions, as shown in Figure 14b. [62, 63] The kink sites on the platinum surface break carbon-carbon bonds, which is an undesirable reaction and, thereby, a poison is added to the reactant mixture in the form of H_2S that blocks the kink sites via strong adsorption. Poisoning of certain active sites to inhibit an undesirable reaction is one of the strategies for developing selective catalysts for specific reactions.

In addition, there are other additives that change the selectivity, like introducing a second metal or an oxide metal interface that has important catalytic activity. The shape selectivity of benzene hydrogenation shows the importance of surface structure for platinum nanoparticle of the same size [24].

8.b. Adsorbate-induced restructuring

Two molecular components, adsorbate-induced restructuring and adsorbate mobility have been elucidated by utilizing high-pressure scanning tunneling microscopy (HP-STM). STM has been a valuable technique in catalytic surface science because it can operate over a wide range of pressures and temperatures, while providing spatial information of individual atoms or molecules in real space (schematic is shown in Figure 15) [13, 64 , 65-69]. Using a HP-STM, one finds that adsorption of a gas (oxygen, hydrogen or carbon monoxide) changes the surface structure of the 110 face of a platinum single crystal, as shown in Figure 16a[70]. Thus, the surface structure changes as the adsorbate forms chemical bonds to make the chemical bond stronger by forming a thermodynamically more stable adsorbate-substrate bond. This surface phenomenon is caused by the increased coverage of different chemisorbed molecules under pressure. The reversibility of adsorbate induced restructuring can readily be observed as shown by a study of hydrogen adsorption on Cu (110).[69] Figure 16b shows STM images of Cu (110) surface before and during H_2 exposure, revealing the adsorbate-induced restructuring into the (1x2) "missing row" structures under high pressure. After evacuating the chamber, the adsorbate-induced restructuring is lifted.

8.c. Adsorbate mobility

The adsorbate mobility has been observed during catalytic turnover by the high-pressure scanning tunneling microscope [65, 71, 72]. While scanning the surface with the speed 100 Å per mm/sec, there is no distinctive feature of the surface during cyclohexene hydrogenation and dehydrogenation or ethylene hydrogenation. The molecules on the surface, which are the reactants, reaction intermediates and the products, are so mobile that they move on the surface faster than the scanning speed of the tunneling tip while the reaction turns over and the products form, as shown in Figure 17. However, if the surface is poisoned using, for example, carbon monoxide the catalytic reaction stops and there is an ordered surface structure formed on the surface indicating the lack of adsorbate mobility that is associated with poisoning. In many cases, which we have already studied, the mobility of adsorbates is required for the catalytic process to occur as the adsorbed reactants must find the active site and that requires mobility on the catalytically reactive surfaces. These studies indicate that the catalytically active surface is dynamic, both the metal and the adsorbates restructure under catalytic reaction conditions.

8.d. Reaction intermediates

Sum frequency generation (SFG) vibrational spectroscopy is a surface-specific technique that was developed in Berkeley and its roots lie in second harmonic generation[14, 64, 73-78]. Figure 18a shows the schematic of high-pressure SFG vibrational spectroscopy combined with the catalytic reaction measurement. In SFG, one or both laser frequencies are tuned and spatially and temporally overlapped. By scanning one of the lasers in the infrared frequency regime we could obtain a sum frequency signal and, thus a vibrational spectra in the visible, as shown in Fig. 18b.

Such a signal is forbidden from a centrosymmetric medium, such as the bulk of face-centered-cubic crystals or an isotropic high pressure gas or a liquid. However, at the surface, the second order susceptibility ($\chi^{(2)}$) of non-zero is allowed, and the surface yields a vibrational spectrum that is monolayer sensitive as depicted in Figure 18c. It is also able to give us vibrational frequencies of adsorbed molecules across pressure range 10-12 orders of magnitude [77, 79].

Using sum frequency generation vibrational spectroscopy, a surface sensitive technique, we can identify reaction intermediates on the surface during catalytic turnover[80-84]. By measuring the turnover rate in addition to taking SFG signals, kinetics of catalytic reactions can be related to reaction intermediates. For example, in the case of ethylene hydrogenation, some of the species, such as ethylidyne and di-σ-bonded ethylene, are spectators and they do not turn over during ethylene hydrogenation [83, 85]. The π-bonded, weakly bound ethylene is present when 4% of a monolayer concentration turns over. Figure 19 shows the species that we see under cyclohexene

hydrogenation/dehydrogenation reaction conditions [86]. During cyclohexene hydrogenation/dehydrogenation, we see three reaction intermediates [84, 87] (1,3-cyclohexadiene, 1,4-cyclohexadiene and the π-allyl molecule), all participate with various concentration, depending on the surface structure in the turnover, to form the product cyclohexene or benzene.

High pressure SFG can be used to study the reaction intermediates on the nanoparticle surfaces. Figure 20a shows the schematic of an SFG experiment on nanoparticles, that are deposited on a prism that allows for totally internal reflection to increase the detection sensitivity [88]. Our recent SFG studies of pyridine hydrogenation using this scheme [89] revealed pyridinium cation ($C_5H_5NH^+$) reaction intermediates on TTAB-covered platinum nanoparticles and the formation of fully hydrogenated piperidine molecules as reaction products in the gas phase, as shown in Figure 20b.

SFG – surface vibrational spectroscopy is able to detect reaction intermediates on the catalytically active surfaces under reaction conditions with are usually different from the reactants and the products. Thus, direct observation of these intermediates gives another tool to obtain information on how reaction selectivity correlates with the molecular structure of the reaction intermediates.

8.e. Surface composition

In bimetallic materials, surface composition is the key factor influencing the catalytic activity and selectivity. Bimetallic nanoparticles bring the new opportunity to study the role of surface composition on the nanometer scale[90-93].

For example, Rh_xPt_{1-x} bimetallic nanoparticles with variable composition (x =0-1) and constant size (9 ± 1 nm) were synthesized by a one-pot polyol synthetic method and the activity of CO oxidation on these bimetallic nanoparticles was studied. It was found that the turnover rate of a pure Rh nanoparticle is 20 times that of a Pt nanoparticle under the reaction conditions used (100 Torr O_2, 40 Torr CO at 180 °C), while Rh_xPt_{1-x} (x =0.2-0.8) exhibit an intermediate activity [28].

In order to probe the importance of surface composition, we studied bimetallic nanoparticles of platinum-rhodium, palladium-platinum and palladium-rhodium nanoparticles using ambient pressure x-ray photoelectron spectroscopy (AP-XPS). The schematic of AP-XPS is shown in Figure 21, which illustrates a differentially pumped electrostatic lens system that refocuses the electrons into the object plane of a standard electron energy analyzer in the high-vacuum region [15, 94]. Details of the beamline and setup can be found elsewhere[95]. The photon energy of the X-ray source was tuned so that the kinetic energy of the detected electrons can be varied. This method permits us to test the surface specific XPS signal and determine the surface composition of bimetallic nanoparticles.

Figures 22a shows the XPS results of 8 nm $Rh_{0.5}Pt_{0.5}$ nanoparticles as a function of kinetic energy of the x-ray, which shows the moderate surface segregation of rhodium. Our preliminary results also indicate that the surface composition changes as the reaction

condition is altered. This result is shown in Figure 22b, which depicts the change of surface composition of $Rh_{0.5}Pt_{0.5}$ bimetallic nanoparticles, suggesting that Rh is pulled to the surface during reaction (oxidizing conditions). The variation of surface composition can be revealed in other bimetallic nanoparticle systems. Figure 22c and 22d show the variation of composition on $Pd_{0.5}Rh_{0.5}$ and $Pd_{0.5}Pt_{0.5}$ bimetallic nanoparticles with size of 16 nm as a function of the kinetic energies of X-ray, indicating these nanoparticles exhibit higher surface composition of rhodium and palladium, respectively. Therefore, the surface composition is different from the bulk composition and this changes the reaction rate and product distribution if both metals participate in the chemistry.

There are bi-functional materials that can be made by synthesizing an oxide or a sulfide coating around a metal nanoparticle. Two-component core-shell systems synthesized based on the Kirkendall effect [96] are also promising multicomponent nanocatalyst systems. TEM images of Pt nanoparticles and Pt/CoO core-shell nanostructures, often called nanoreactors are shown in Figure 23 [97]. These systems promise to be highly selective in reactions where active sites, both on the oxide and the metal, are important to produce the desired product, as long as metal core is accessible to reactants and reaction products through the porous oxide shell.

8.f. Charge Transport

Many studies starting back in the 1950's by Schwab and coworkers, indicate that the oxide-metal interface is a very active catalytic site [31]. It was found that the activity was enhanced under methane oxidation ($CH_4 + 2O_2 \rightarrow CO_2 + 2H_2O$) on ZnO/Ag metal-oxide mixed catalysts, as shown in Figure 24a [32]. They found that the mixed catalyst exhibits a much higher activity than ZnO or Ag of the same weight and, quote, "The most striking factor is that the mixed catalyst gives an extremely high yield in water vapor and carbon dioxide" and also, quote, "The catalytic promoter effect in a mixed catalyst is traced back to an electron exchange between support and catalyst." [32].

After Schwab's finding, a whole group of catalysts called "strong metal support interaction (SMSI) materials" have been reported to exhibit catalytic activity and selectivity changes as the oxide metal interface changes [33, 98, 99]. These materials covers the group VIII metals Fe, Ni, Rh, Pt, Pd, and Ir supported on certain oxides (TiO_x, TaO_x, CeO_x, and NbO_x). For example, it was reported by G.L. Haller et al. that methane formation from CO or CO_2 and H_2 is enhanced by three orders of magnitude on a SMSI material [33 , 100]. Figure 24b is the AFM image of a platinum nanoparticle fabricated using a lithography technique where the chemically active oxide-metal interface was highlighted [35, 36].

The origin of the oxide–metal support interaction has been attributed to either geometric or electronic effects [8, 33, 101]. The geometrical effect assumes that the active surface area of the noble metal is changed during the reduction process. The electronic effect involves charge transfer between the metal and the oxide support. Elucidation of the origin of the metal-support interaction requires measurement of the charge transfer

through the oxide–metal interface. This effect was also investigated by Boffa and others using various oxides deposited on rhodium [102]. They observed a remarkable 14-fold increase in turnover rates for CO_2 hydrogenation, especially in the presence of three different oxides: TiO_x, NbO_x. and TaO_x. The activity was at a maximum when the oxide-metal interface area was at a maximum, which occurred at about one-half of a monolayer of oxide coverage. Recently, hot electron generation during exothermic reaction conditions or in the presence of photons reveals probable reasons for the change of chemical activity due to the oxide metal interface [2, 38, 41, 59, 103-106].

During exothermic chemical processes, energetic charge carriers can be generated through the non-adiabatic electronic dissipation of chemical energy. Experimental evidence indicating the presence of energetic electrons, known as "hot" electrons, has been reported. Pump-probe experiments carried out on femtosecond time scales detect the presence of electrons with kinetic energies of 1-3 eV that have elastic mean free paths of approximately 10 nm in metals. Several experiments suggest that the electronic excitation causes atomic/molecular processes, such as adsorption/desorption or molecular dissociation. Nienhaus et al. detected electrons with a kinetic energy greater than 0.5 eV injected into their diode when hydrogen or oxygen atoms adsorbed on a silver thin film Schottky diode. The hot electrons travel in excess of the ~20 nm electron mean free path in silver and surmount the ~ 0.5 eV Schottky barrier formed at the junction of silver and the underlying semiconductor [40, 41, 107].

. To detect this flow of hot electrons, we fabricated a metal-semiconductor Schottky diode [38, 39, 106, 108]. If the metal particle [59] or film [109] is of the diameter or thickness of the electron mean free path (~10 nm), hot electrons can be collected as they

are transported across the metal without collision, as shown in Fig. 25a. For an n-type Schottky diode, hot electrons are detected as a chemicurrent if their excess energy E_{ex}= $|E-E_F|$ is larger than the effective Schottky barrier, which is the difference between the conduction band minimum and the Fermi energy, E_F, at the interface. Once hot electrons arrive at the oxide, they dissipate energy and, thus, cannot go back to the metal. Therefore, the Schottky energy barrier leads to an irreversible, one-way charge transfer of hot electrons from the metal to semiconductor. After hot electrons move from metal to semiconductor, they are replaced by low energy electrons supplied by the external leads connected to the Pt and semiconductor, resulting in a continuous flow of hot electrons generated by the catalytic reaction.

The catalytic nanodiode consists of a 5 nm platinum thin film formed on a semiconducting film (titanium dioxide or gallium nitride) with gold pads for Ohmic contact to the Pt and semiconductor. Figure 25b shows the schematic of the Pt/GaN diode. We found that the hot electron flow is correlated with the turnover rate of CO oxidation measured on the Pt/GaN diode, as shown in Figure 25c [109, 110]. This experiment clearly verifies that the chemical energy in the catalytic reaction is converted to the electron kinetic energy of the hot electron flows.

8.g. Oxidation states

When we synthesized platinum and rhodium nanoparticles using dendrimers as a support we could produce nanoparticles around 1 nm or smaller in size. The oxide component is more prevalent for the smaller nanoparticles [22]. Since the oxidation state changes the chemistry, this size dependence of the oxidation state introduces new

chemistry for small clusters of atoms, which may approach the behavior of homogeneous catalysts [111-114]. Figures 26a and 26b show XPS results of Pt_{20} (0.8 nm in size) and Pt_{40} (1.5 nm in size), respectively, indicating that the oxidation states of these small, non-metallic nanoparticles depend on the particle size [55]. In case of Pt_{20}, The ratio of Pt^{x+} /Pt(0) is 13, indicating that the Pt4f peak is mainly dominated by the oxidation state. By controlling the oxidation state by the size of the cluster these clusters could be used to approach the chemistry known for homogeneous catalyst such as hydroformylation and carbonylation reactions to mention two important classes of homogeneous catalysts. Future studies will test how one may prepare homogeneous catalysts by depositing size-controlled metal clusters in dendrimers or other supports, thereby making it easier to separate the catalysts that are heterogeneous from the reactants and products.

9. Future Perspective

We call the field nanocatalysis when it uses mono-dispersed metal nanoparticles with controlled size and shape and when it involves synthesis, characterization and reaction studies on both two and three dimensions. This vertical integration of catalysis science speeds up the development of the field at a time when energy efficiency and chemical selectivity (green chemistry) are major societal goals. A new generation of young scientists are being trained who could carry out synthesis, characterization and reaction studies, all by the same person. These we call "Homo Catalyticus" because the same individual carries out all three aspects of catalytic studies., which were partitioned in the past. This way, the same person can use the knowledge gained by reaction studies of how to change synthesis and how to characterize what has been found successfully when producing selective catalysts via controlled fabrication. This approach not only accelerates research progress put permits the rapid transfer of results using model systems to catalyst design for the chemical technologies. Already new generations of industrial catalysts being produced using the approach of model system studies. Example are the new methanol synthesis Cu/ZnO catalyst and a new generation hydrodesulfurization catalyst from the Haldor Topsoe company [115-117] and the new generation of catalytic converters that appear on automobiles because of gains in selectivity, turnover rates and perhaps resistance to deactivation industry is likely to convert from catalyst fabrication that was pioneered by Mittasch in the 1920's [118] to high technology fabrication methods that are suggested by model nanocatalyst studies. There is need to develop nanocatalyst model systems for other reaction conditions such as high reaction temperatures (such as

combustion and cracking) and at solid-liquid interfaces. These challenges have not been addressed in this paper.

The nanomaterial technology that allows one to make catalysts from 1-10 nm in size and shape, that are fully controlled, allows us to dream about bringing together the three fields of catalysis: enzyme, homogeneous and heterogeneous. Since enzymes mostly operate at temperatures around 300 Kelvin and in solution (which is most often aqueous, although organic solvents work frequently), it would be important that we carry out catalytic reaction studies using heterogeneous, enzymes and homogeneous catalysts at room temperature and in solution. This way, one can perhaps correlate molecular components of the three catalyst types and develop hybrid systems that take advantage of, for example, enzyme selectivity in a heterogeneous medium. The future is indeed bright for catalysis science viewed from the perspective of nanocatalysis.

Acknowledgement

This paper is based on the plenary lecture presented at the International Symposium on Creation and Control of Advanced Selective Catalysis, Kyoto, Japan. This work was supported by the Director, Office of Science, Office of Basic Energy Sciences, Division of Materials Sciences and Engineering of the U.S. Department of Energy under Contract No. DE-AC02-05CH11231.

Table 1. Toolbox for studying two-dimensional or three-dimensional nanoparticles.

Ex-situ Characterization
Transmission Electron Microscopy (TEM) X-ray Diffraction (XRD) Diffuse Reflectance UV-Vis Spectroscopy X-ray Photoelectron Spectroscopy (XPS) Scanning Electron Microscopy (SEM) Chemisorption, Physisorption Small Angle X-ray Scattering (SAXS) Energy Dispersive X-ray Analysis (EDX) Thermogravimetric Analysis (TGA) Temperature Programmed Oxidation (TPO) Inductively Coupled Plasma – Optical Emission Spectroscopy (ICP-OES)
Spectroscopies and Microscopy for in-situ characterization
High-Pressure Scanning tunneling microscopy (HP-STM) High-Pressure Sum Frequency Generation Spectroscopy (HP-SFG) Ambient-Pressure X-ray Photoelectron Spectroscopy (APXPS) Diffuse Reflectance Infrared Spectroscopy (DRIFTS) UV-Raman and Surface Enhanced Raman Spectroscopy (SERS) Transmission electron microscopy (TEM) Tapered element oscillating microbalance (TEOM) thermogravimetric analysis (TGA) UV-Vis diffuse reflectance spectroscopy X-ray diffraction (XRD) Small-Angle/Wide-Angle X-ray Scattering (SAXS-WAXS)

Figure Captions

Figure 1. A one dimensional potential energy plot illustrating selectivity in heterogeneous catalysis. Relative heights among activation barriers for different reactions determine the selectivity of catalytic processes [17].

Figure 2. Most heterogeneous, enzyme and homogeneous catalysts are nanoparticles. (a) The cytochrome c molecule. (b) Titanium-based single site homogeneous polymerization catalyst. (c) scanning electron microscopy (SEM) image of 8 nm monodispersed Pt/Rh bimetallic nanoparticles deposited on silicon substrate.

Figure 3. Evolution of model surface systems from single crystal surface to nanoparticles, nanowires and nanodiodes.

Figure 4. Schematic of one-step synthesis of monodispersed rhodium nanoparticles

Figure 5. Platinum monodispersed nanoparticles of 1–7 nm size and well-controlled cubic or cuboctahedral shapes.

Figure 6. Synthesis of dendrimers capped monodispersed platinum nanoparticles of cluster sizes of one nm or less.

Figure 7. (a) TEM image of two-dimensional (2D) TTAB coated platinum nanoparticle arrays and (b) TEM image of three-dimensional (3D) platinum nanoparticle encapsulated in mesoporous silica (SBA-15).

Figure 8. (a) Schematic of catalytic batch reactor for studies of small area 2D catalysts, and (b) flow reactors for studies of three-dimensional high surface area catalyst systems.

Figure 9. The size dependence of Pt nanoparticles on the selectivity of cyclohexene hydrogenation/dehydrogenation, and (b) crotonaldehyde hydrogenation.

Figure 10. Turnover rates of cyclohexene and cyclohexane formation under benzene hydrogenation on Pt (111) and Pt(100) surface, and cubic and cuboctahedra platinum nanoparticles, demonstrating the similarities between the single crystal and nanoparticle surfaces.

Scheme 1. Schematics of multi-path reactions that are used for understanding molecular selectivity. (a) Benzene hydrogenation, (b) cyclohexene hydrogenation/dehydrogenation, (c) crotonaldehyde hydrogenation, and (d) pyrrole hydrogenation.

Figure 11. The size dependence of Pt nanoparticles encapsulated by dendrimer on the selectivity of pyrrole hydrogenation. Selectivity was measured under 4 Torr of pyrrole, 400 Torr of H^2, and at 413 K.

Figure 12. Turnover rates of nanoparticle arrays during CO oxidation (100 Torr of O_2 and 40 Torr of CO) with different capping layers measured at 513 K.

Figure 13. SFG spectrum of (a) Oleylamine capped 10 nm Pt nanoparticles (10 nm), (b) spectrum of Pt nanoparticles after removal of the organic capping by UV-ozone exposure for 200 minutes and (c) spectrum of benzene adsorbed on the platinum nanoparticle surfaces after removal of the organic capping.

Scheme 2. Seven molecular components influencing reaction selectivity.

Figure 14. (a) High pressure-ultra high vacuum combined system. The high-pressure cell is shown in both the open (top) and closed (bottom) positions. (b)

Structure sensitivity of alkane aromatization and light alkane skeletal rearrangements are revealed.

Figure 15. The schematic of high pressure STM.

Figure 16. (a) In-situ STM images reveal adsorbate-induced restructuring of Pt (110) surface in 1.7 atm hydrogen (73 nm x 70 nm), 1.0 atm oxygen (90 nm x 78 nm) and 1.0 atm carbon monoxide (77 nm x 74 nm). (b) STM topographical images showing Cu (110) (i) before and (ii) during H_2 exposure. At hydrogen pressures larger than 2 mbar the Cu(110) surface reconstructs into the (1x2) "missing row" structures. (iii) After evacuating, the adsorbate-induced restructuring is lifted and only a (1 x 1) surface structure is revealed with STM [from reference [69]].

Figure 17. 10 nm x 10 nm STM images of a Pt (111) surface after the subsequent addition of 20 mTorr H_2, 20 mTorr of C_2H_4, and 5.6 mTorr of CO.

Figure 18. (a) Schematic of high pressure SFG system, a vibrational spectroscopic tool for probing the adsorbed species during the catalytic reaction. (b) The frequency ω_{vis} of the visible laser beam is kept fixed, and the IR-beam frequency ω_{IR} is varied. When ω_{IR} coincides with a vibrational transition from $|0>$ to $|1>$ of an adsorbed molecule, the molecule is excited to a virtual state $|n>$ and emits the sum frequency ω_{SFG}. (c) Because of selection rule, SFG signal is forbidden from a centrosymmetric medium.

Figure 19. SFG spectra of cyclohexene hydrogenation to cyclohexane and dehydrogenation to benzene. These two reactions occur simultaneously in excess hydrogen of about 10 Torr and 1.5 Torr of hydrocarbon. SFG vibration spectra reveals that the presence of three different species on the surface in this reactant mixture, 1,4-, 1,3-cyclohexadienes and π-allyl c-C_6H_9, that are reaction intermediates.

Figure 20. (a) Schematic of in-situ monitoring of nanoparticles with high pressure sum frequency generation (SFG) spectroscopy. (b) pyridinium cation ($C_5H_5NH^+$) reaction intermediates is present under reaction condition of pyridine hydrogenation to piperidine.

Figure 21. Schematic of ambient pressure x-ray photoelectron spectroscopy [15, 94].

Figure 22. (a) XPS results of 8 nm $Rh_{0.5}Pt_{0.5}$ nanoparticles as a function of kinetic energy of the x-ray, which shows the moderate surface segregation of rhodium. (b) XPS results under high pressure condition indicates greater surface segregation of rhodium during reaction (oxidizing) conditions. The kinetic energy of X-ray is 300 eV, and 60 mTorr of CO and 150 mTorr of O_2 were used for the high pressure experiment. (c) Rh has the higher surface composition for $Rh_{0.5}Pd_{0.5}$ bimetallic nanoparticles, while (d) Pd has the higher surface composition for $Pt_{0.5}Pd_{0.5}$ bimetallic nanoparticles.

Figure 23. Schematic of synthesis of Pt/CoO core-shell nanostructures and TEM images of Pt nanoparticles and Pt/CoO core-shell nanoparticles [from reference [97]]. The scale bars in TEM images are 50 nm.

Figure 24. (a) Plot of partial pressure of CO_2 under methane oxidation on ZnO/Ag mixed catalyst, ZnO, and Ag in the same weight [32]. (b) AFM image of platinum nanoparticle fabricated with lithography technique. Oxide-metal interface is highlighted.

Figure 25. (a) Scheme of the detection of ballistic charge carrier in the catalytic metal-semiconductor Schottky diode. (b) Schematic of Pt/GaN nanodiode device. (c) Chemicurrent and turnover rate as a function of temperature during carbon monoxide oxidation reveal the correlation between the hot electron flows and catalytic reactions.

Figure 26. XPS results of (a) Pt_{20} (0.8 nm in size) and (b) Pt_{40} nanoparticles (1.5 nm in size). The ratio of Pt^{x+} /Pt(0) of Pt_{20} and Pt_{40} nanoparticles are 13 and 0.16, respectively, suggesting that the higher oxidation state of Pt in Pt_{20} is dominant.

References

[1] G. A. Somorjai, *Introduction to Surface Chemistry and Catalysis, Wiley, New York,* **1994**.

[2] G. A. Somorjai, K. M. Bratlie, M. O. Montano, J. Y. Park, *Journal of Physical Chemistry B* **2006**, *110*, 20014.

[3] G. A. Somorjai, J. Y. Park, *Catalysis Letters* **2007**, *115*, 87.

[4] J. H. Clark, *Green Chemistry* **1999**, *1*, 1.

[5] A. Corma, *Chemical Reviews* **1997**, *97*, 2373.

[6] C. T. Kresge, M. E. Leonowicz, W. J. Roth, J. C. Vartuli, J. S. Beck, *Nature* **1992**, *359*, 710.

[7] D. Zhao, P. Yang, N. Melosh, J. Feng, B. F. Chmelka, G. D. Stucky, *Advanced Materials* **1998**, *10*, 1380.

[8] K. Hayek, M. Fuchs, B. Klotzer, W. Reichl, G. Rupprechter, *Topics in Catalysis* **2000**, *13*, 55.

[9] R. Narayanan, M. A. El-Sayed, *Nano Letters* **2004**, *4*, 1343.

[10] Y. Borodko, S. M. Humphrey, T. D. Tilley, H. Frei, G. A. Somorjai, *Journal of Physical Chemistry C* **2007**, *111*, 6288.

[11] H. Song, F. Kim, S. Connor, G. A. Somorjai, P. D. Yang, *Journal of Physical Chemistry B* **2005**, *109*, 188.

[12] G. A. Somorjai, J. Y. Park, *Journal of Chemical Physics* **2008**, *128*.

[13] K. B. Rider, K. S. Hwang, M. Salmeron, G. A. Somorjai, *Journal of the American Chemical Society* **2002**, *124*, 5588.

[14] Y. R. Shen, *Nature* **1989**, *337*, 519.

[15] M. Salmeron, R. Schlogl, *Surface Science Reports* **2008**, *63*, 169.

[16] G. A. Somorjai, J. Y. Park, *Physics Today* **2007**, *60*, 48.

[17] F. Zaera, *Journal of Physical Chemistry B* **2002**, *106*, 4043.

[18] G. A. Somorjai, Y. G. Borodko, *Catalysis Letters* **2001**, *76*, 1.

[19] P. B. Weisz, *Pure and Applied Chemistry* **1980**, *52*, 2091.

[20] G. A. Somorjai, M. C. Yang, *Topics in Catalysis* **2003**, *24*, 61.

[21] G. A. Somorjai, R. M. Rioux, *Catalysis Today* **2005**, *100*, 201.

[22] I. Balint, A. Miyazaki, K. Aika, *Journal of Catalysis* **2003**, *220*, 74.

[23] C. Mohr, H. Hofmeister, J. Radnik, P. Claus, *Journal of the American Chemical Society* **2003**, *125*, 1905.

[24] K. M. Bratlie, H. Lee, K. Komvopoulos, P. Yang, G. A. Somorjai, *Nano Letters* **2007**, *7*, 3097.

[25] G. Ertl, H. J. Freund, *Physics Today* **1999**, *52*, 32.

[26] W. S. Caughey, G. A. Smythe, D. H. Okeeffe, J. E. Maskasky, M. L. Smith, *Journal of Biological Chemistry* **1975**, *250*, 7602.

[27] N. Tian, Z. Y. Zhou, S. G. Sun, Y. Ding, Z. L. Wang, *Science* **2007**, *316*, 732.

[28] J. Y. Park, Y. Zhang, M. Grass, T. Zhang, G. A. Somorjai, *Nano Letters* **2008**, *8*, 673

[29] H. J. Freund, H. Kuhlenbeck, J. Libuda, G. Rupprechter, M. Baumer, H. Hamann, *Topics in Catalysis* **2001**, *15*, 201.

[30] G. A. Somorjai, R. L. York, D. Butcher, J. Y. Park, *Physical Chemistry Chemical Physics* **2007**, *9*, 3500.

[31] G. M. Schwab, *Angewandte Chemie-International Edition* **1967**, *6*, 375.
[32] G. M. Schwab, K. Koller, *Journal of the American Chemical Society* **1968**, *90*, 3078.
[33] G. L. Haller, D. E. Resasco, *Advances in Catalysis* **1989**, *36*, 173.
[34] G. A. Somorjai, F. Tao, J. Y. Park, *Topics in Catalysis* **2008**, *47*, 1.
[35] J. Grunes, J. Zhu, E. A. Anderson, G. A. Somorjai, *Journal of Physical Chemistry B* **2002**, *106*, 11463.
[36] J. Grunes, J. Zhu, M. C. Yang, G. A. Somorjai, *Catalysis Letters* **2003**, *86*, 157.
[37] X. M. Yan, A. M. Contreras, M. M. Koebel, J. A. Liddle, G. A. Somorjai, *Nano Letters* **2005**, *5*, 1129.
[38] X. Z. Ji, G. A. Somorjai, *Journal of Physical Chemistry B* **2005**, *109*, 22530.
[39] X. Z. Ji, A. Zuppero, J. M. Gidwani, G. A. Somorjai, *Journal of the American Chemical Society* **2005**, *127*, 5792.
[40] H. Nienhaus, H. S. Bergh, B. Gergen, A. Majumdar, W. H. Weinberg, E. W. McFarland, *Physical Review Letters* **1999**, *82*, 446.
[41] H. Nienhaus, B. Gergen, W. H. Weinberg, E. W. McFarland, *Surface Science* **2002**, *514*, 172.
[42] Y. Zhang, M. E. Grass, S. E. Habas, F. Tao, T. Zhang, P. Yang, G. A. Somorjai, *Journal of Physical Chemistry C* **2007**, *111*, 12243.
[43] R. M. Rioux, H. Song, M. Grass, S. Habas, K. Niesz, J. D. Hoefelmeyer, P. Yang, G. A. Somorjai, *Topics in Catalysis* **2006**, *39*, 167.
[44] H. Lee, S. E. Habas, S. Kweskin, D. Butcher, G. A. Somorjai, P. D. Yang, *Angewandte Chemie-International Edition* **2006**, *45*, 7824.
[45] Y. W. Zhang, M. E. Grass, J. N. Kuhn, F. Tao, S. E. Habas, W. Y. Huang, P. D. Yang, G. A. Somorjai, *Journal of the American Chemical Society* **2008**, *130*, 5868.
[46] S. M. Humphrey, M. E. Grass, S. E. Habas, K. Niesz, G. A. Somorjai, T. D. Tilley, *Nano Letters* **2007**, *7*, 785.
[47] M. E. Grass, Y. Yue, S. E. Habas, R. M. Rioux, C. I. Teall, P. Yang, G. A. Somorjai, *Journal of Physical Chemistry C* **2008**, *112*, 4797.
[48] H. Song, R. M. Rioux, J. D. Hoefelmeyer, R. Komor, K. Niesz, M. Grass, P. D. Yang, G. A. Somorjai, *Journal of the American Chemical Society* **2006**, *128*, 3027.
[49] G. A. Somorjai, J. Y. Park, *Topics in Catalysis* **2008**, in press.
[50] R. M. Crooks, M. Q. Zhao, L. Sun, V. Chechik, L. K. Yeung, *Accounts of Chemical Research* **2001**, *34*, 181.
[51] Y. H. Niu, L. K. Yeung, R. M. Crooks, *Journal of the American Chemical Society* **2001**, *123*, 6840.
[52] Y. Li, M. A. El-Sayed, *Journal of Physical Chemistry B* **2001**, *105*, 8938.
[53] K. R. Gopidas, J. K. Whitesell, M. A. Fox, *Nano Letters* **2003**, *3*, 1757.
[54] R. W. J. Scott, O. M. Wilson, R. M. Crooks, *Journal of Physical Chemistry B* **2005**, *109*, 692.
[55] W. Huang, J. N. Kuhn, C. K. Tsung, Y. Zhang, S. E. Habas, P. Yang, G. A. Somorjai, *Nano Letters* **2008**, *8*, 2027.
[56] D. Y. Zhao, J. L. Feng, Q. S. Huo, N. Melosh, G. H. Fredrickson, B. F. Chmelka, G. D. Stucky, *Science* **1998**, *279*, 548.
[57] P. Schmidt-Winkel, W. W. Lukens, D. Y. Zhao, P. D. Yang, B. F. Chmelka, G. D. Stucky, *Journal of the American Chemical Society* **1999**, *121*, 254.

[58] K. M. Bratlie, C. J. Kliewer, G. A. Somorjai, *Journal of Physical Chemistry B* **2006**, *110*, 17925.
[59] J. Y. Park, H. Lee, J. R. Renzas, Y. Zhang, G. A. Somorjai, *Nano Letters* **2008**, *8*, 2388.
[60] J. R. Vig, *Journal of Vacuum Science & Technology a-Vacuum Surfaces and Films* **1985**, *3*, 1027.
[61] C. Aliaga, J. Y. Park, Y. Yamada, G. A. Somorjai, *(unpublished)*.
[62] S. M. Davis, F. Zaera, G. A. Somorjai, *Journal of the American Chemical Society* **1982**, *104*, 7453.
[63] G. A. Somorjai, *Reaction Kinetics and Catalysis Letters* **1987**, *35*, 37.
[64] G. A. Somorjai, X. C. Su, K. R. McCrea, K. B. Rider, *Topics in Catalysis* **1999**, *8*, 23.
[65] M. Montano, M. Salmeron, G. A. Somorjai, *Surface Science* **2006**, *600*, 1809.
[66] M. Montano, D. C. Tang, G. A. Somorjai, *Catalysis Letters* **2006**, *107*, 131.
[67] S. R. Longwitz, J. Schnadt, E. K. Vestergaard, R. T. Vang, E. Laegsgaard, I. Stensgaard, H. Brune, F. Besenbacher, *Journal of Physical Chemistry B* **2004**, *108*, 14497.
[68] B. L. M. Hendriksen, J. W. M. Frenken, *Physical Review Letters* **2002**, *89*.
[69] L. Osterlund, P. B. Rasmussen, P. Thostrup, E. Laegsgaard, I. Stensgaard, F. Besenbacher, *Physical Review Letters* **2001**, *86*, 460.
[70] B. J. McIntyre, M. Salmeron, G. A. Somorjai, *Journal of Vacuum Science & Technology a-Vacuum Surfaces and Films* **1993**, *11*, 1964.
[71] M. Montano, K. Bratlie, M. Salmeron, G. A. Somorjai, *Journal of the American Chemical Society* **2006**, *128*, 13229.
[72] D. C. Tang, K. S. Hwang, M. Salmeron, G. A. Somorjai, *Journal of Physical Chemistry B* **2004**, *108*, 13300.
[73] G. Rupprechter, *Mrs Bulletin* **2007**, *32*, 1031.
[74] Y. R. Shen, *Annual Review of Physical Chemistry* **1989**, *40*, 327.
[75] K. Y. Kung, P. Chen, F. Wei, Y. R. Shen, G. A. Somorjai, *Surface Science* **2000**, *463*, L627.
[76] O. Mermut, D. C. Phillips, R. L. York, K. R. McCrea, R. S. Ward, G. A. Somorjai, *Journal of the American Chemical Society* **2006**, *128*, 3598.
[77] X. C. Su, P. S. Cremer, Y. R. Shen, G. A. Somorjai, *Journal of the American Chemical Society* **1997**, *119*, 3994.
[78] S. Westerberg, C. Wang, G. A. Somorjai, *Surface Science* **2005**, *582*, 137.
[79] X. C. Su, J. Jensen, M. X. Yang, M. B. Salmeron, Y. R. Shen, G. A. Somorjai, *Faraday Discussions* **1996**, *105*, 263.
[80] K. M. Bratlie, L. D. Flores, G. A. Somorjai, *Journal of Physical Chemistry B* **2006**, *110*, 10051.
[81] Z. Chen, D. H. Gracias, G. A. Somorjai, *Applied Physics B-Lasers and Optics* **1999**, *68*, 549.
[82] P. Cremer, C. Stanners, J. W. Niemantsverdriet, Y. R. Shen, G. Somorjai, *Surface Science* **1995**, *328*, 111.
[83] P. S. Cremer, X. C. Su, Y. R. Shen, G. A. Somorjai, *Catalysis Letters* **1996**, *40*, 143.

[84] M. Yang, G. A. Somorjai, *Journal of the American Chemical Society* **2003**, *125*, 11131.
[85] P. S. Cremer, X. C. Su, Y. R. Shen, G. A. Somorjai, *Journal of the American Chemical Society* **1996**, *118*, 2942.
[86] K. M. Bratlie, L. D. Flores, G. A. Somorjai, *Surface Science* **2005**, *599*, 93.
[87] M. C. Yang, R. M. Rioux, G. A. Somorjai, *Journal of Catalysis* **2006**, *237*, 255.
[88] S. J. Kweskin, R. M. Rioux, S. E. Habas, K. Komvopoulos, P. Yang, G. A. Somorjai, *Journal of Physical Chemistry B* **2006**, *110*, 15920.
[89] K. M. Bratlie, K. Komvopoulos, G. A. Somorjai, unpublished.
[90] L. E. Aleandri, H. Bonnemann, D. J. Jones, J. Richter, J. Roziere, *Journal of Materials Chemistry* **1995**, *5*, 749.
[91] J. A. Rodriguez, D. W. Goodman, *Science* **1992**, *257*, 897.
[92] J. Rothe, G. Kohl, J. Hormes, H. Bonnemann, W. Brijoux, K. Siepen, *Journal De Physique Iv* **1997**, *7*, 959.
[93] N. Toshima, T. Yonezawa, *New Journal of Chemistry* **1998**, *22*, 1179.
[94] H. Bluhm, M. Havecker, A. Knop-Gericke, M. Kiskinova, R. Schlogl, M. Salmeron, *Mrs Bulletin* **2007**, *32*, 1022.
[95] D. F. Ogletree, H. Bluhm, G. Lebedev, C. S. Fadley, Z. Hussain, M. Salmeron, *Review of Scientific Instruments* **2002**, *73*, 3872.
[96] A. D. Smigelskas, E. O. Kirkendall, *Transactions of the American Institute of Mining and Metallurgical Engineers* **1947**, *171*, 130.
[97] Y. D. Yin, R. M. Rioux, C. K. Erdonmez, S. Hughes, G. A. Somorjai, A. P. Alivisatos, *Science* **2004**, *304*, 711.
[98] S. J. Tauster, S. C. Fung, R. L. Garten, *Journal of the American Chemical Society* **1978**, *100*, 170.
[99] K. Foger, *in: Catalysis, Science and Technology eds. J.R. Anderson and M. Boudart, Vol. 6 (Springer-Verlag, Berlin, 1984) ch. 4.*
[100] J. P. Hindermann, G. J. Hutchings, A. Kiennemann, *Catalysis Reviews-Science and Engineering* **1993**, *35*, 1.
[101] R. Burch, *in: Hydrogen Effects in Catalysis, eds. Z. Pa´al and P.G.Menon (Dekker, New York, 1988) p. 347.*
[102] A. Boffa, C. Lin, A. T. Bell, G. A. Somorjai, *Journal of Catalysis* **1994**, *149*, 149.
[103] Y. H. Huang, C. T. Rettner, D. J. Auerbach, A. M. Wodtke, *Science* **2000**, *290*, 111.
[104] J. W. Gadzuk, *Journal of Physical Chemistry B* **2002**, *106*, 8265.
[105] H. Nienhaus, S. J. Weyers, B. Gergen, E. W. McFarland, *Sensors and Actuators B-Chemical* **2002**, *87*, 421.
[106] J. Y. Park, G. A. Somorjai, *Journal of Vacuum Science & Technology B* **2006**, *24*, 1967.
[107] H. Nienhaus, *Surface Science Reports* **2002**, *45*, 3.
[108] J. Y. Park, J. R. Renzas, A. M. Contreras, G. A. Somorjai, *Topics in Catalysis* **2007**, *46*, 217.
[109] J. Y. Park, J. R. Renzas, B. B. Hsu, G. A. Somorjai, *Journal of Physical Chemistry C* **2007**, *111*, 15331.
[110] J. Y. Park, G. A. Somorjai, *Chemphyschem* **2006**, *7*, 1409.

[111] M. D. Ackermann, T. M. Pedersen, B. L. M. Hendriksen, O. Robach, S. C. Bobaru, I. Popa, C. Quiros, H. Kim, B. Hammer, S. Ferrer, J. W. M. Frenken, *Physical Review Letters* **2005**, *95*.
[112] M. S. Chen, Y. Cal, Z. Yan, K. K. Gath, S. Axnanda, D. W. Goodman, *Surface Science* **2007**, *601*, 5326.
[113] H. Gabasch, A. Knop-Gericke, R. Schlogl, M. Borasio, C. Weilach, G. Rupprechter, S. Penner, B. Jenewein, K. Hayek, B. Klotzer, *Physical Chemistry Chemical Physics* **2007**, *9*, 533.
[114] N. Lopez, T. V. W. Janssens, B. S. Clausen, Y. Xu, M. Mavrikakis, T. Bligaard, J. K. Norskov, *Journal of Catalysis* **2004**, *223*, 232.
[115] J. D. Grunwaldt, A. M. Molenbroek, N. Y. Topsoe, H. Topsoe, B. S. Clausen, *JOURNAL OF CATALYSIS* **2000**, *194*, 452.
[116] N. Y. Topsoe, H. Topsoe, *TOPICS IN CATALYSIS* **1999**, *8*, 267.
[117] K. G. Knudsen, B. H. Cooper, H. Topsoe, *APPLIED CATALYSIS A-GENERAL* **1999**, *189*, 205.
[118] A. Mittasch, E. Keunecke, *ZEITSCHRIFT FUR ELEKTROCHEMIE UND ANGEWANDTE PHYSIKALISCHE CHEMIE* **1932**, *38*, 666.

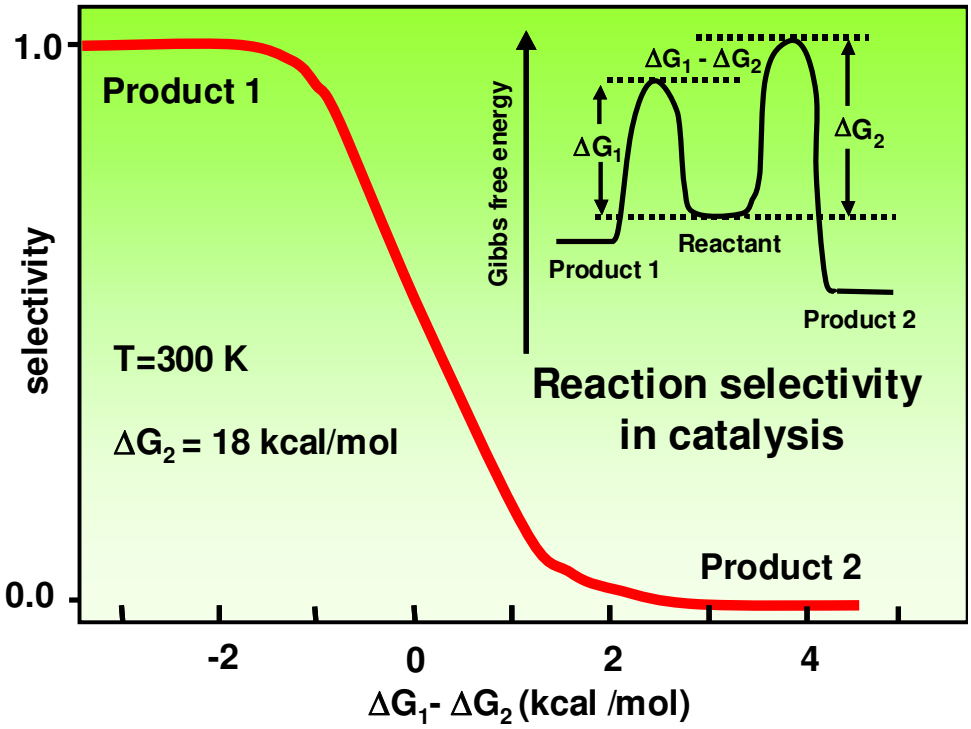
1.0
0.0
selectivity
Product 1
T=300 K
ΔG2 = 18 kcal/mol
Product 2
Reaction selectivity
in catalysis
Gibbs free energy
ΔG1 - ΔG2
ΔG1
ΔG2
Reactant
Product 1
Product 2
-2
0
2
4
ΔG1- ΔG2 (kcal /mol)

Figure 1.

(a) Enzyme

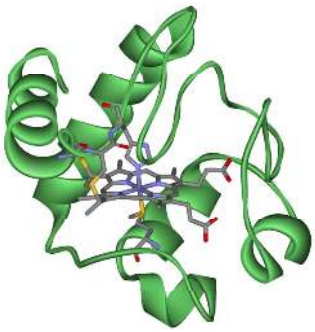

Cytochrome C
Size: ~4 nm, 100 amino acids
Molecular weight: ~12,000 daltons

(b) Homogeneous catalysis

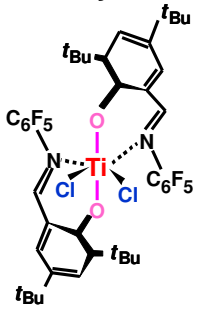

Single-site olefin polymerization catalyst
Size : ~1.6 nm

(c) Heterogeneous catalysis

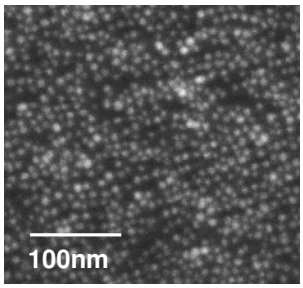

Pt/Rh bimetallic nanoparticles
Size : 8 nm

Figure 2.

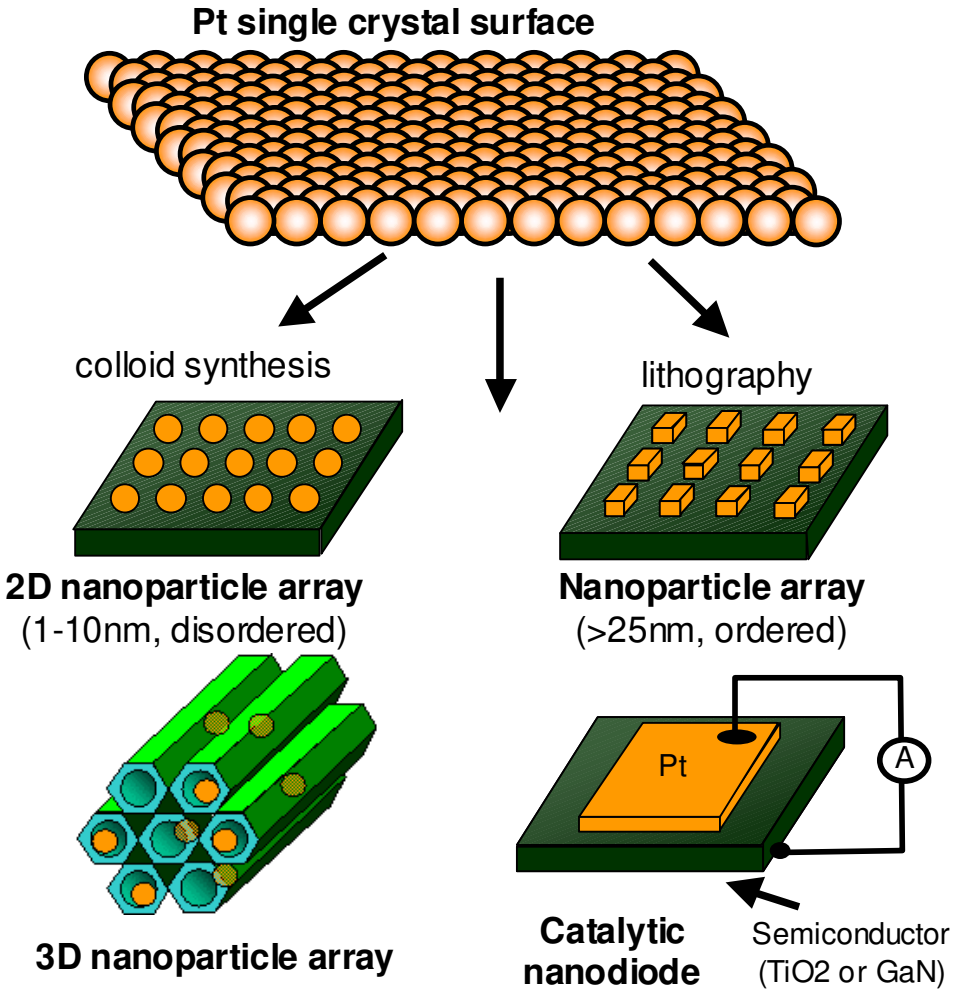
Pt single crystal surface
colloid synthesis
lithography
2D nanoparticle array
(1-10nm, disordered)
Nanoparticle array
(>25nm, ordered)
3D nanoparticle array
Pt
A
Catalytic
nanodiode
Semiconductor
(TiO2 or GaN)

Figure 3.

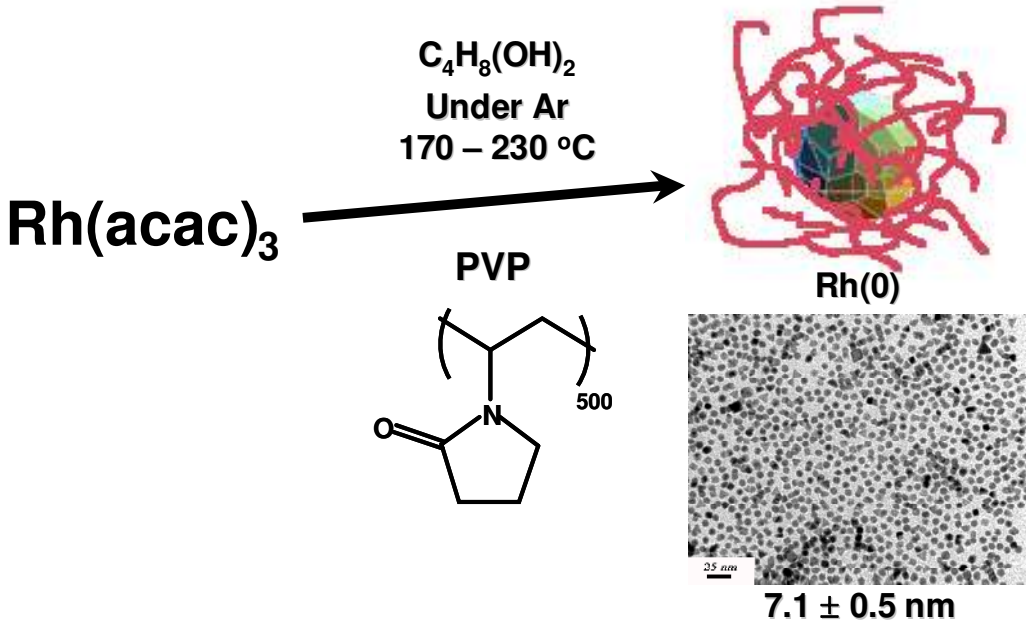

Figure 4.

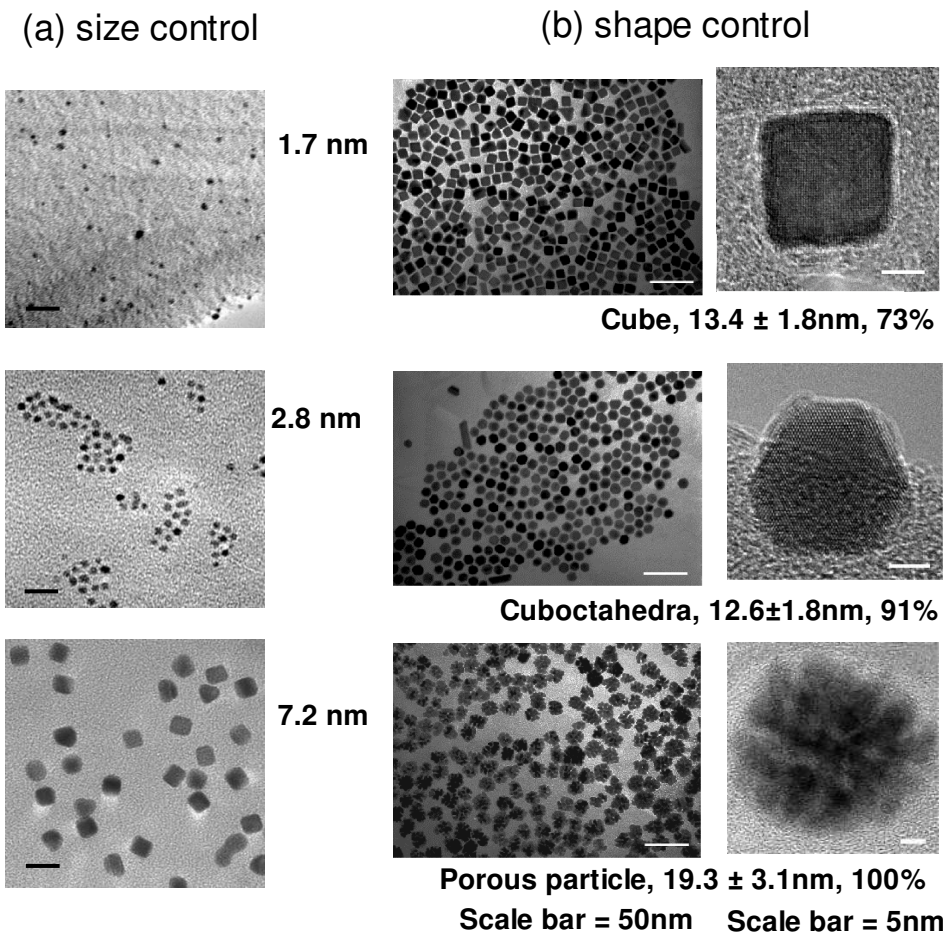
(a) size control
(b) shape control
1.7 nm
2.8 nm
7.2 nm
Cube, 13.4 ± 1.8nm, 73%
Cuboctahedra, 12.6±1.8nm, 91%
Porous particle, 19.3 ± 3.1nm, 100%
Scale bar = 50nm
Scale bar = 5nm

Figure 5.

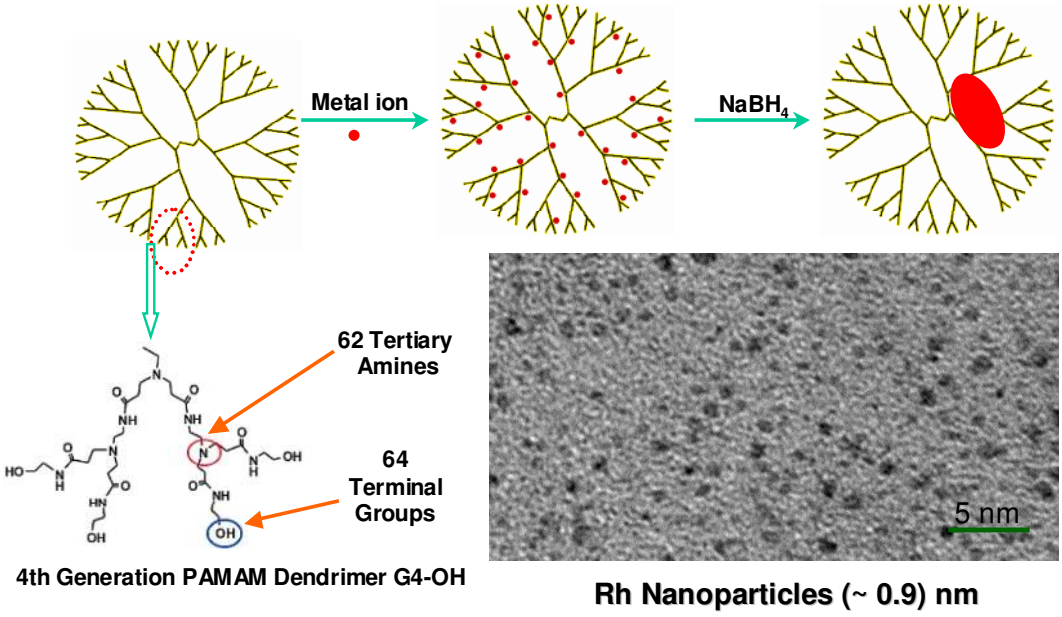
Metal ion
NaBH4
62 Tertiary Amines
64 Terminal Groups
4th Generation PAMAM Dendrimer G4-OH
5 nm
Rh Nanoparticles (~ 0.9) nm

Figure 6.

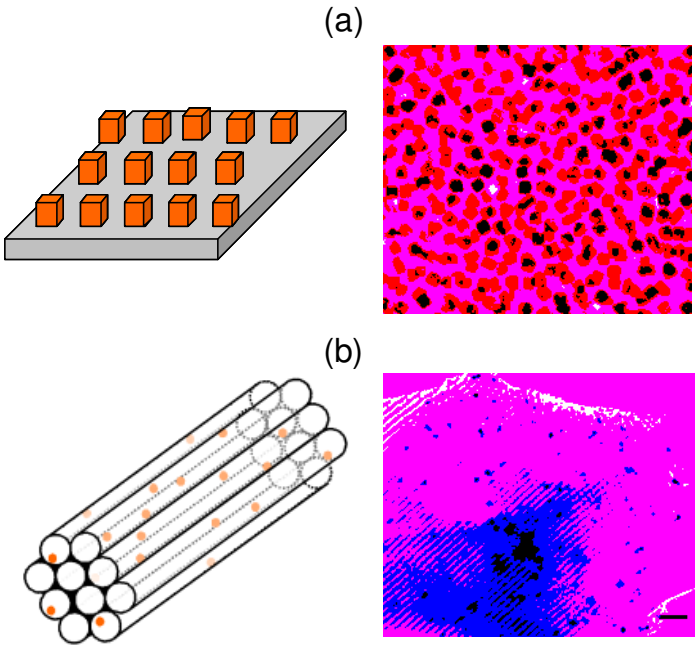

Figure 7.

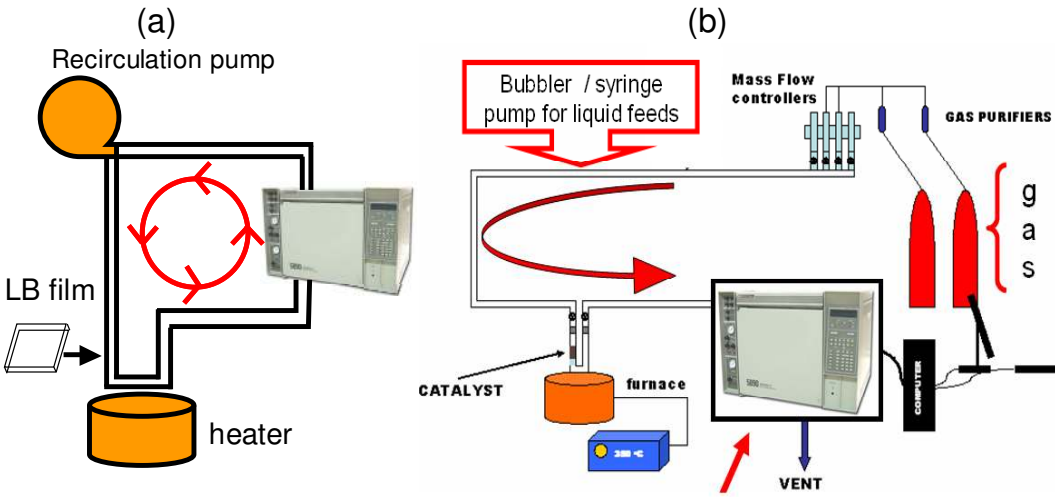
(a)
Recirculation pump
LB film
heater
(b)
Bubbler / syringe pump for liquid feeds
Mass Flow controllers
GAS PURIFIERS
g
a
s
CATALYST
furnace
COMPUTER
VENT

Figure 8.

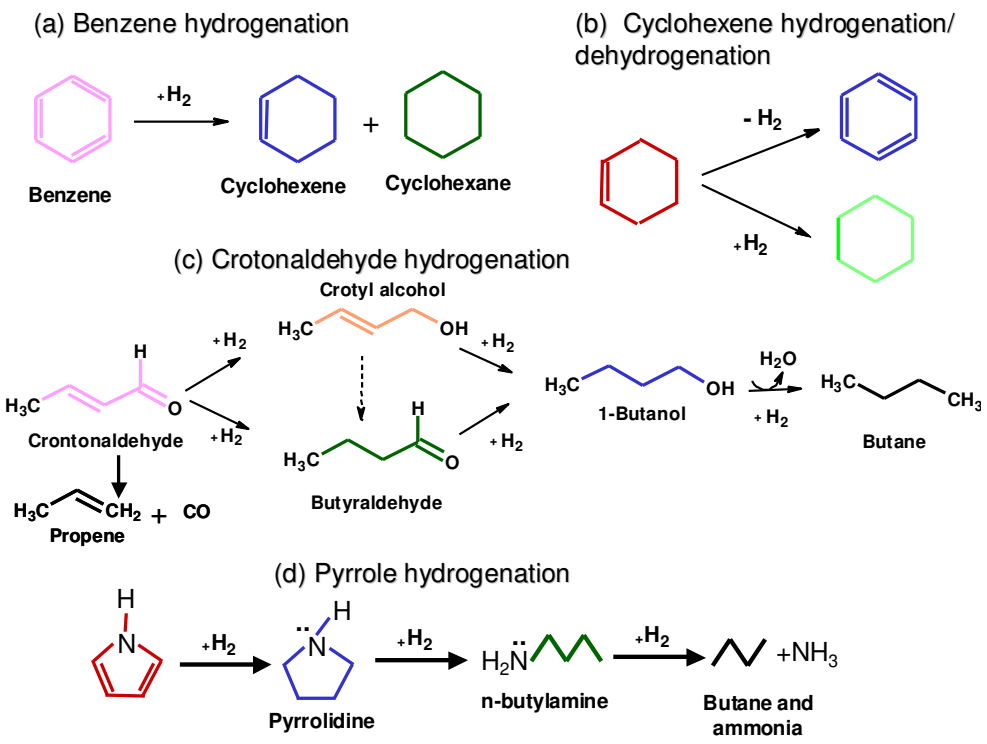
(a) Benzene hydrogenation
+H2
Benzene
Cyclohexene
Cyclohexane
(b) Cyclohexene hydrogenation/ dehydrogenation
- H2
+H2
(c) Crotonaldehyde hydrogenation
Crotyl alcohol
H3C
OH
+H2
H
O
Crontonaldehyde
Butyraldehyde
1-Butanol
H2O
Butane
CH3
CH2
CO
Propene
(d) Pyrrole hydrogenation
N
Pyrrolidine
H2N
n-butylamine
+NH3
Butane and ammonia

Scheme 1.

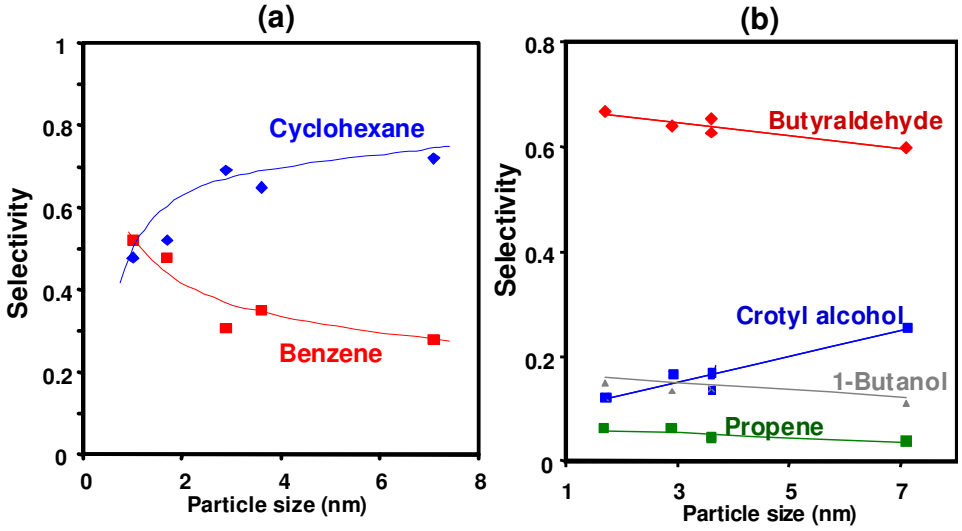
(a)
Selectivity
Particle size (nm)
Cyclohexane
Benzene
(b)
Selectivity
Particle size (nm)
Butyraldehyde
Crotyl alcohol
1-Butanol
Propene

Figure 9.

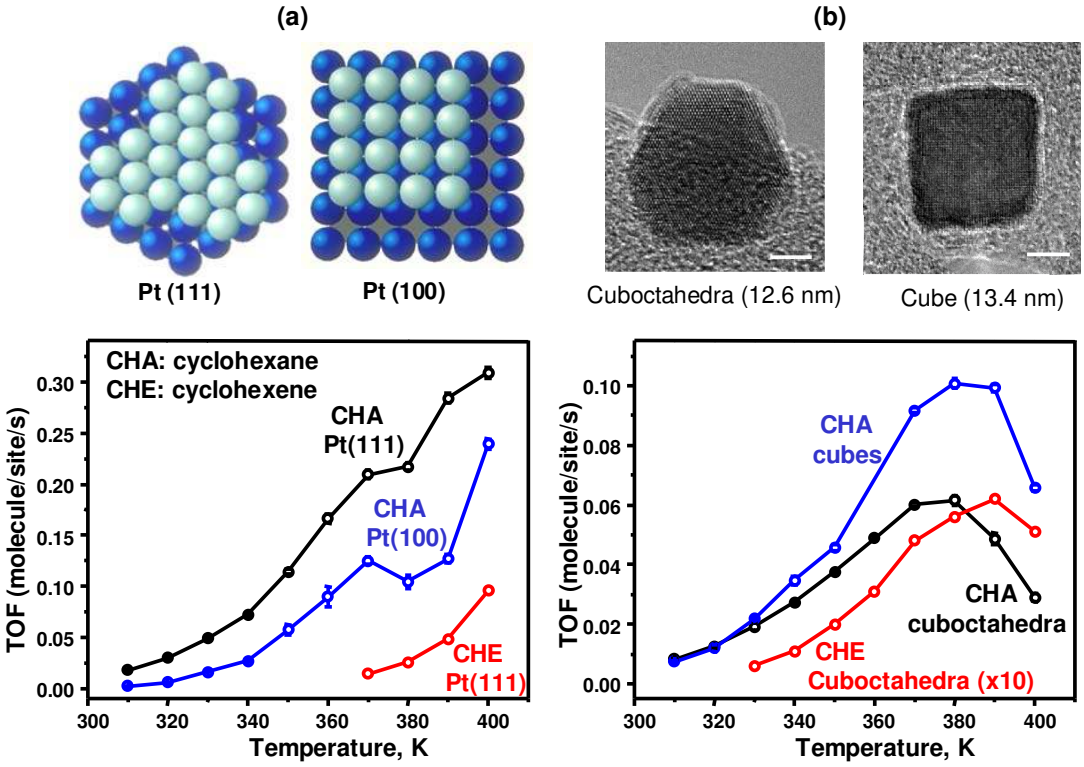
(a)
(b)
Pt (111)
Pt (100)
Cuboctahedra (12.6 nm)
Cube (13.4 nm)
CHA: cyclohexane
CHE: cyclohexene
CHA
Pt(111)
CHA
Pt(100)
CHE
Pt(111)
TOF (molecule/site/s)
Temperature, K
CHA
cubes
CHA
cuboctahedra
CHE
Cuboctahedra (x10)
TOF (molecule/site/s)
Temperature, K

Figure 10.

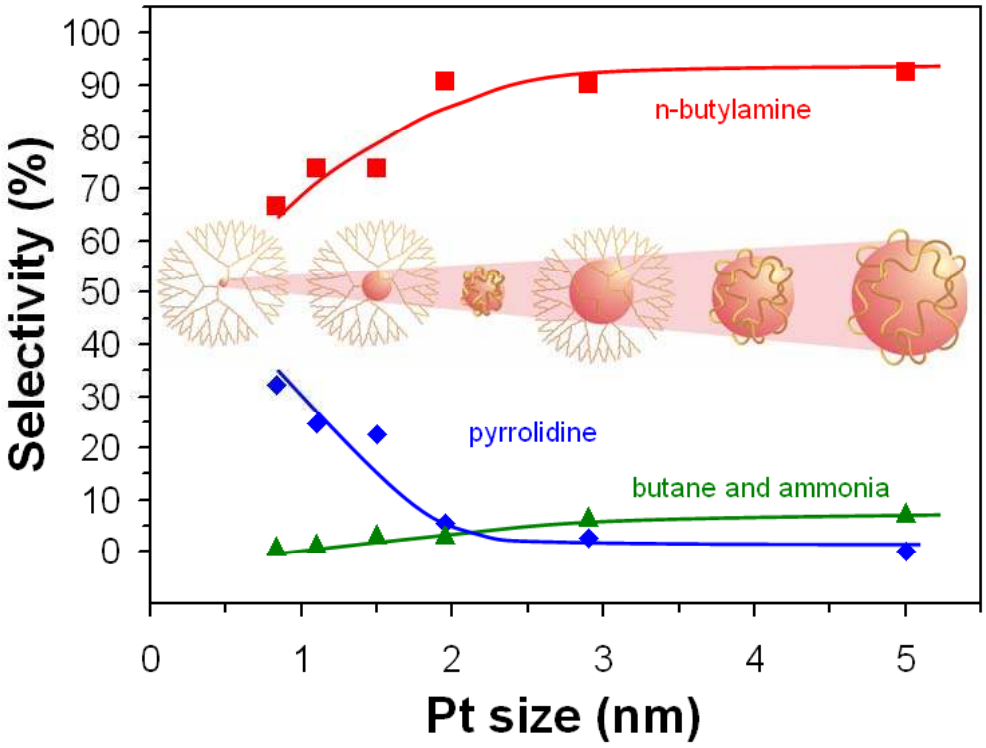
Selectivity (%)
100
90
80
70
60
50
40
30
20
10
0
0
1
2
3
4
5
Pt size (nm)
n-butylamine
pyrrolidine
butane and ammonia

Figure 11.

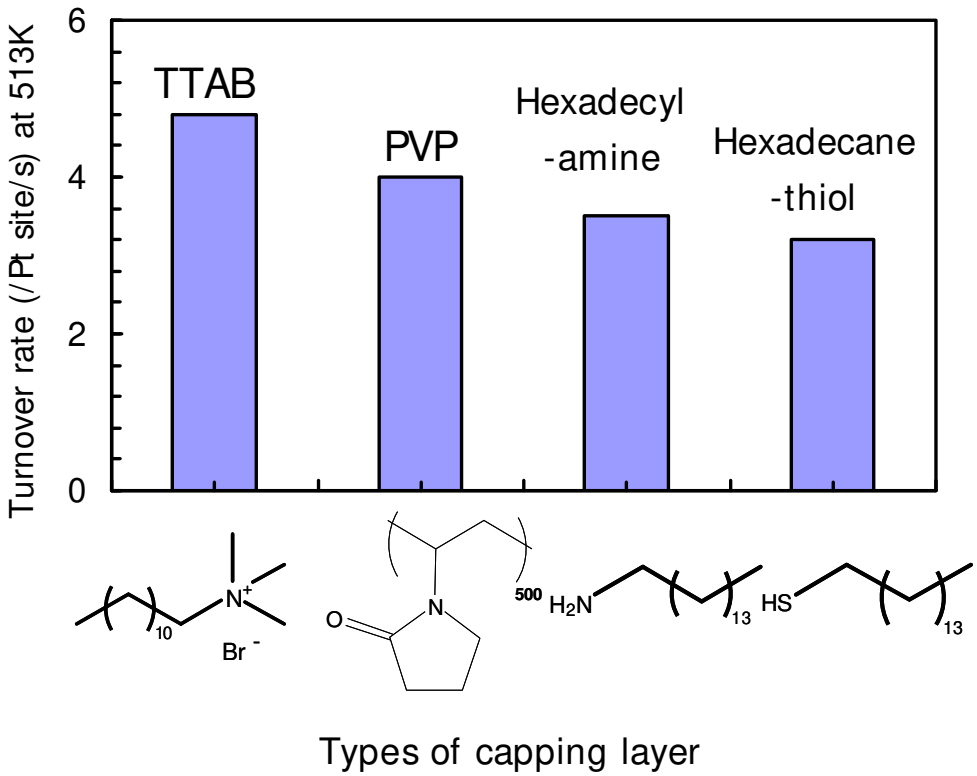
Turnover rate (/Pt site/s) at 513K
6
4
2
0
TTAB
PVP
Hexadecyl
-amine
Hexadecane
-thiol
N+
10
Br -
O
N
500
H2N
13
HS
13
Types of capping layer

Figure 12.

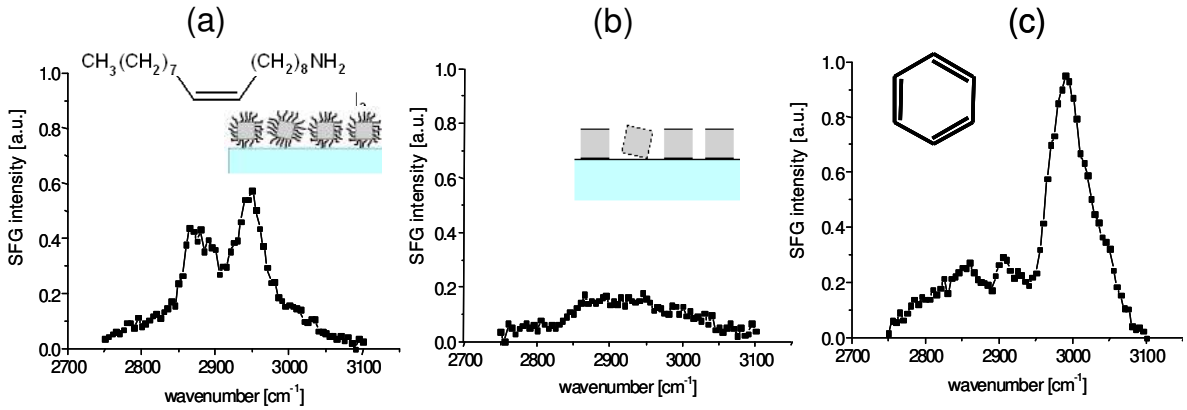
(a)
(b)
(c)
$CH_3(CH_2)_7$
$(CH_2)_8NH_2$
SFG intensity [a.u.]
wavenumber [cm^{-1}]
1.0
0.8
0.6
0.4
0.2
0.0
2700
2800
2900
3000
3100

Figure 13.

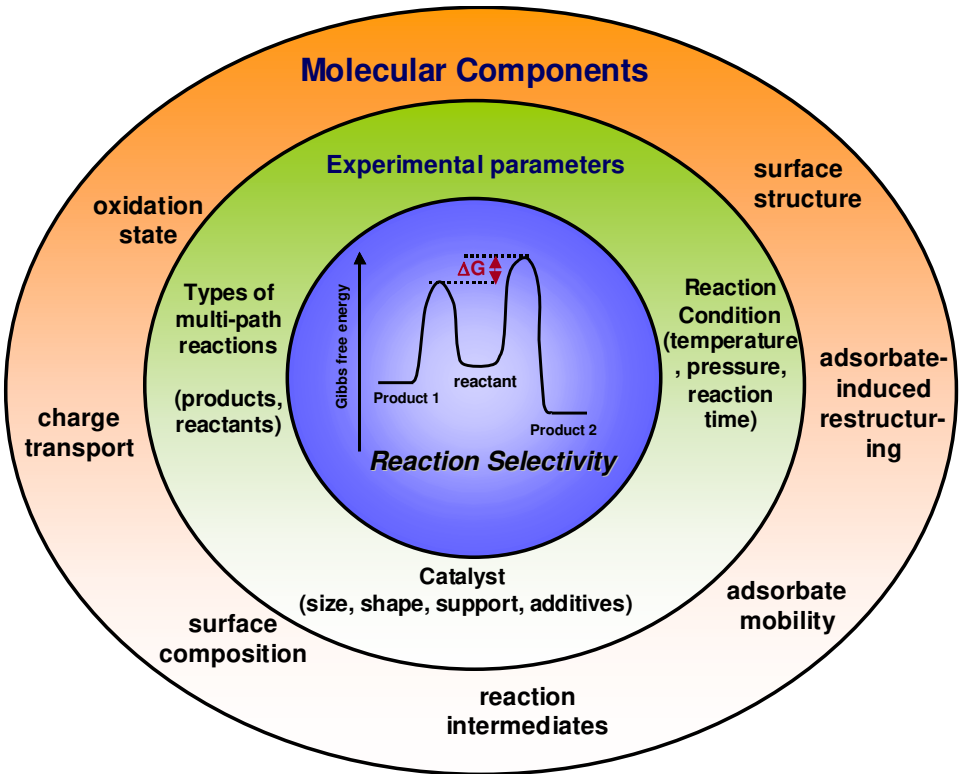
Molecular Components
Experimental parameters
oxidation state
surface structure
Types of multi-path reactions
(products, reactants)
Reaction Condition (temperature, pressure, reaction time)
charge transport
adsorbate-induced restructur-ing
ΔG
Gibbs free energy
reactant
Product 1
Product 2
Reaction Selectivity
Catalyst
(size, shape, support, additives)
adsorbate mobility
surface composition
reaction intermediates

Scheme 2.

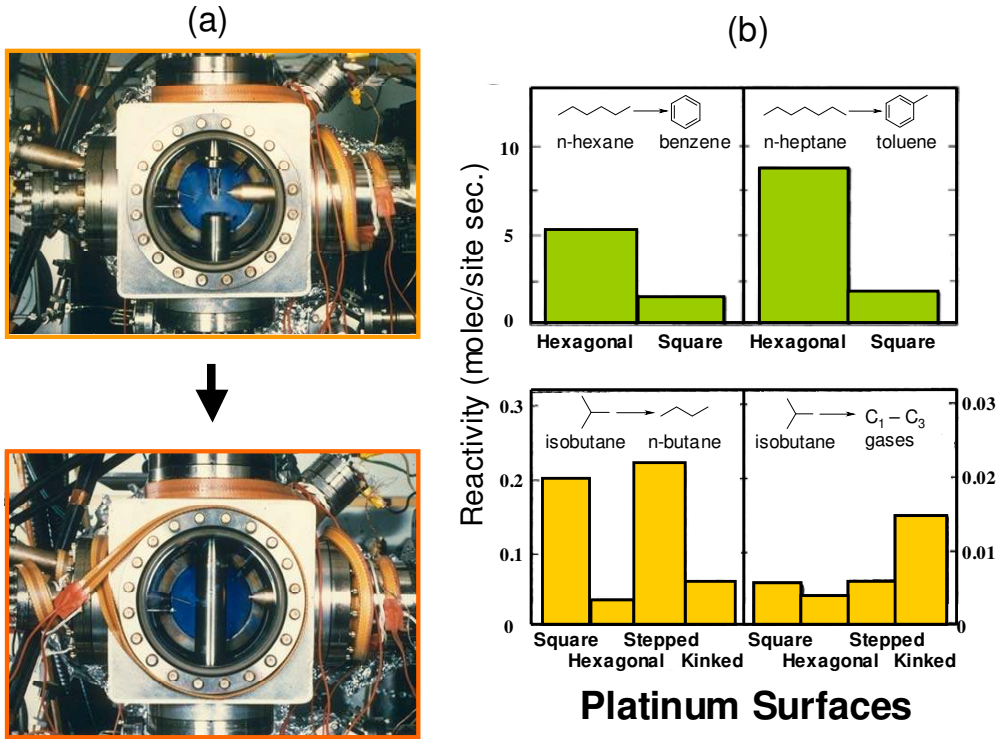
(a)
(b)
n-hexane
benzene
n-heptane
toluene
10
5
0
Hexagonal
Square
Hexagonal
Square
Reactivity (molec/site sec.)
0.3
0.2
0.1
0
isobutane
n-butane
isobutane
C1 – C3
gases
0.03
0.02
0.01
0
Square
Hexagonal
Stepped
Kinked
Square
Hexagonal
Stepped
Kinked
Platinum Surfaces

Figure 14.

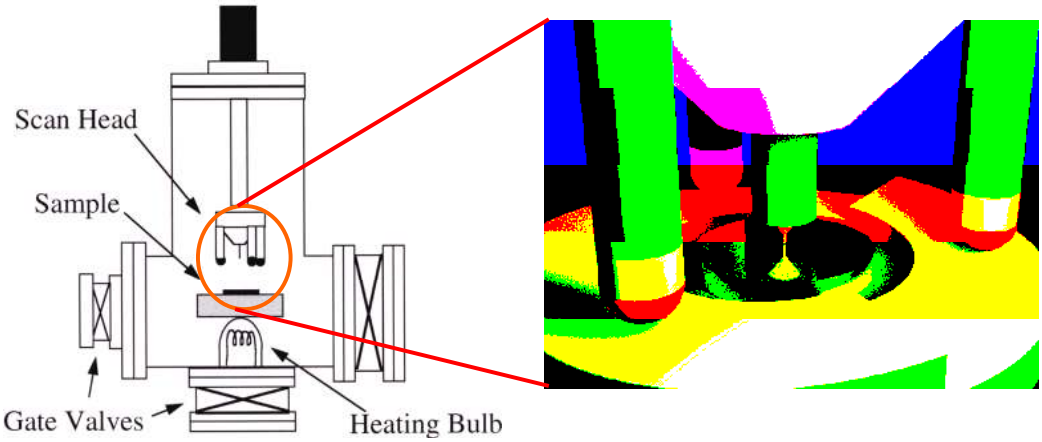

Figure 15.

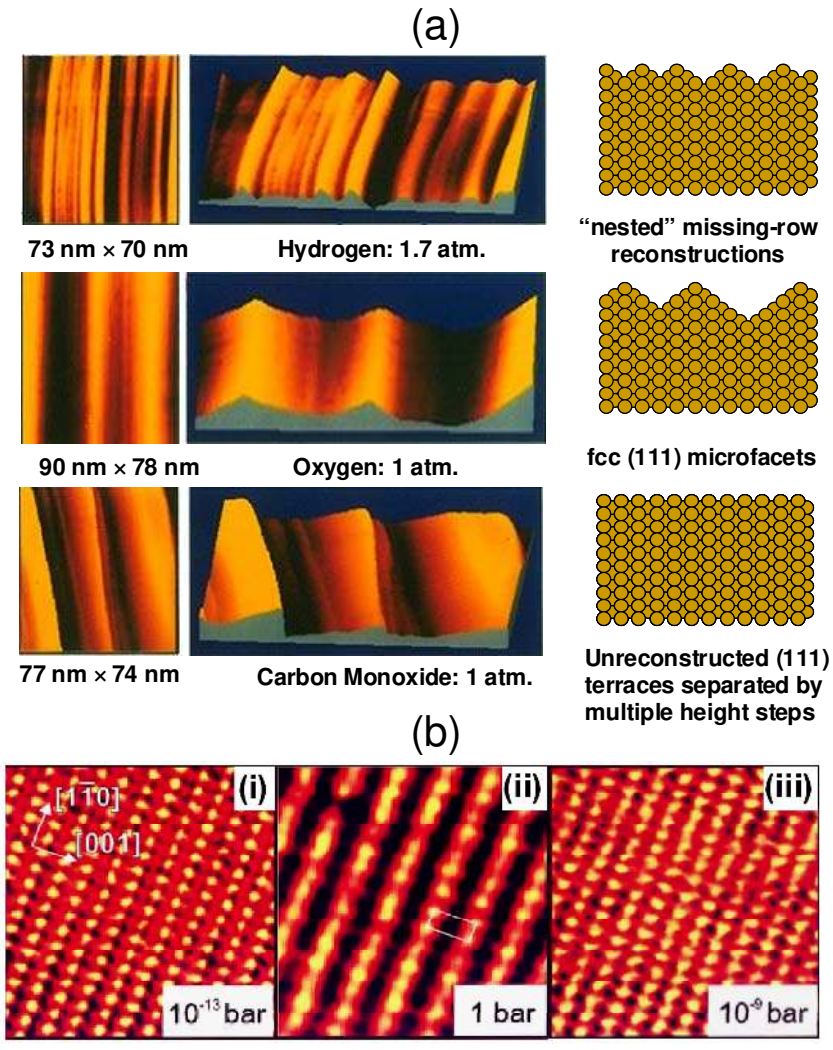
(a)
73 nm × 70 nm
Hydrogen: 1.7 atm.
"nested" missing-row reconstructions
90 nm × 78 nm
Oxygen: 1 atm.
fcc (111) microfacets
77 nm × 74 nm
Carbon Monoxide: 1 atm.
Unreconstructed (111) terraces separated by multiple height steps
(b)
[1$\bar{1}$0]
[001]
(i)
10^{-13} bar
(ii)
1 bar
(iii)
10^{-9} bar

Figure 16.

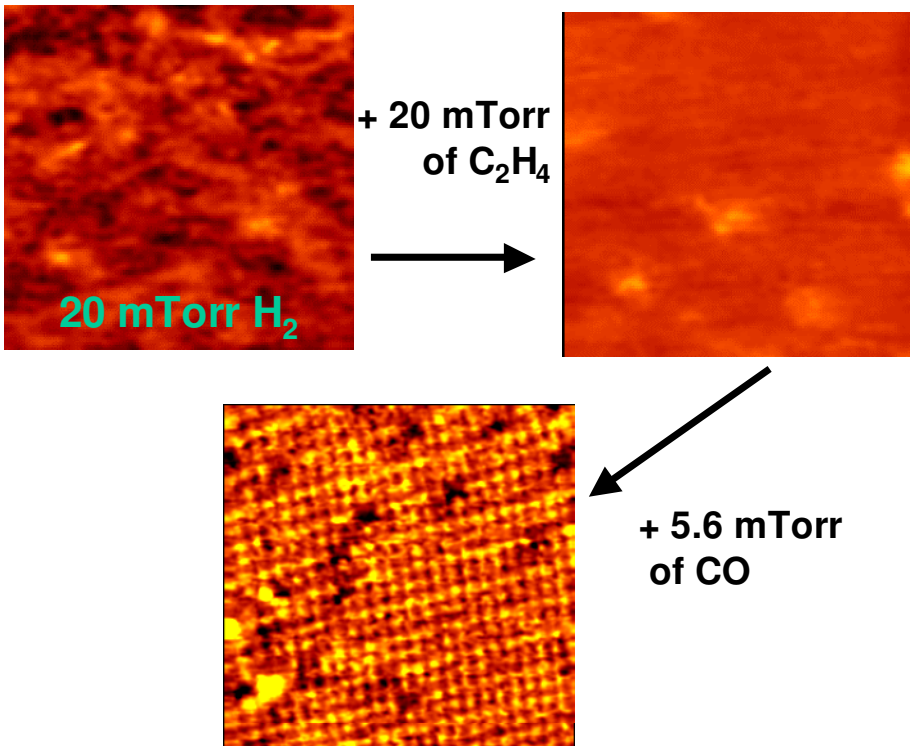

Figure 17.

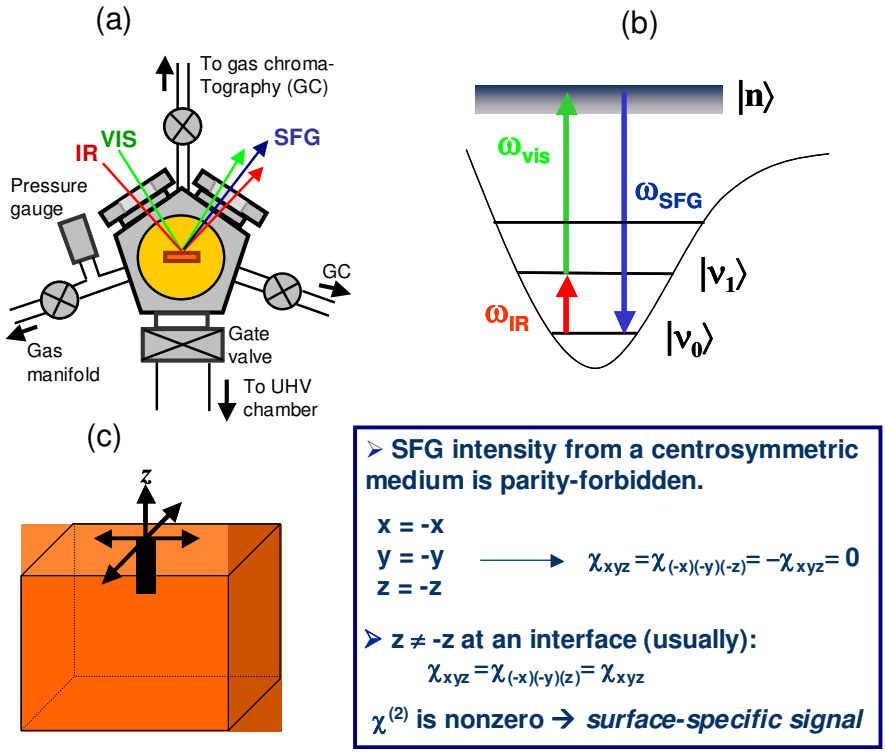
(a)
To gas chroma-
Tography (GC)
IR
VIS
SFG
Pressure
gauge
GC
Gas
manifold
Gate
valve
To UHV
chamber
(b)
|n⟩
ω_vis
ω_SFG
|ν_1⟩
ω_IR
|ν_0⟩
(c)
z
➢ SFG intensity from a centrosymmetric medium is parity-forbidden.
x = -x
y = -y
z = -z
χ_xyz = χ_(-x)(-y)(-z) = −χ_xyz = 0
➢ z ≠ -z at an interface (usually):
χ_xyz = χ_(-x)(-y)(z) = χ_xyz
χ^(2) is nonzero → surface-specific signal

Figure 18.

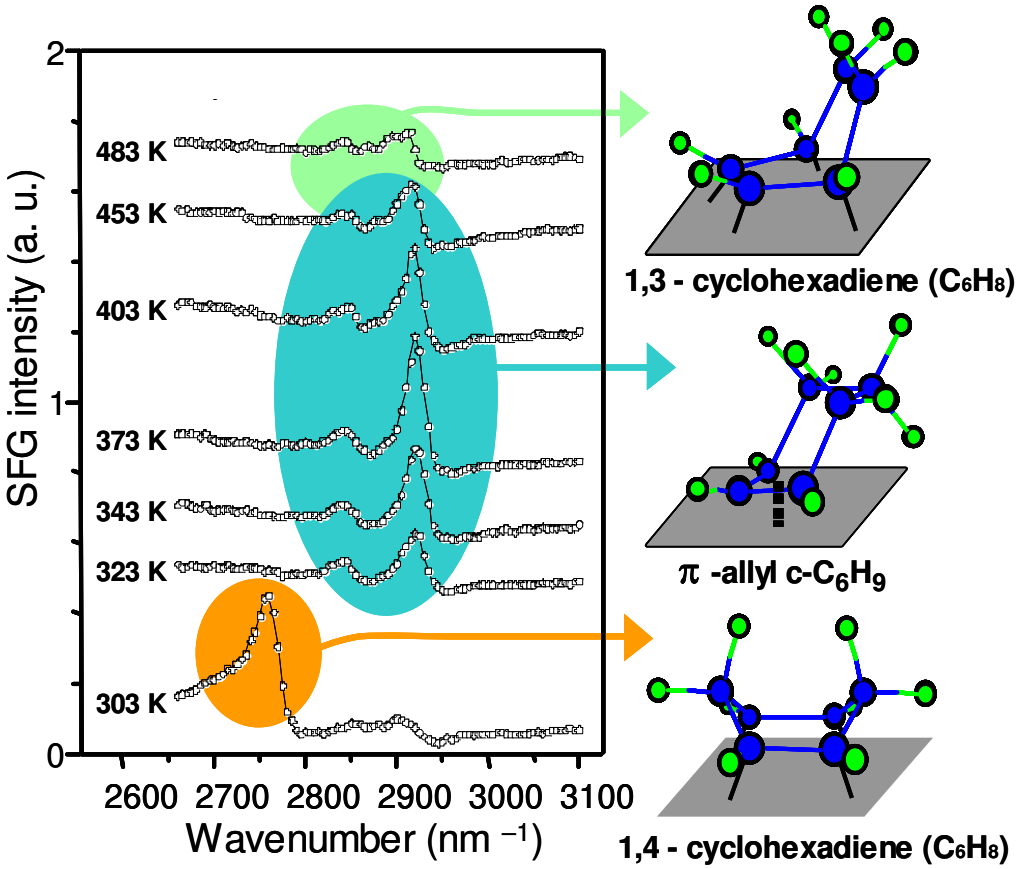
SFG intensity (a. u.)
2
1
0
483 K
453 K
403 K
373 K
343 K
323 K
303 K
2600 2700 2800 2900 3000 3100
Wavenumber (nm −1)
1,3 - cyclohexadiene (C6H8)
π -allyl c-C6H9
1,4 - cyclohexadiene (C6H8)

Figure 19.

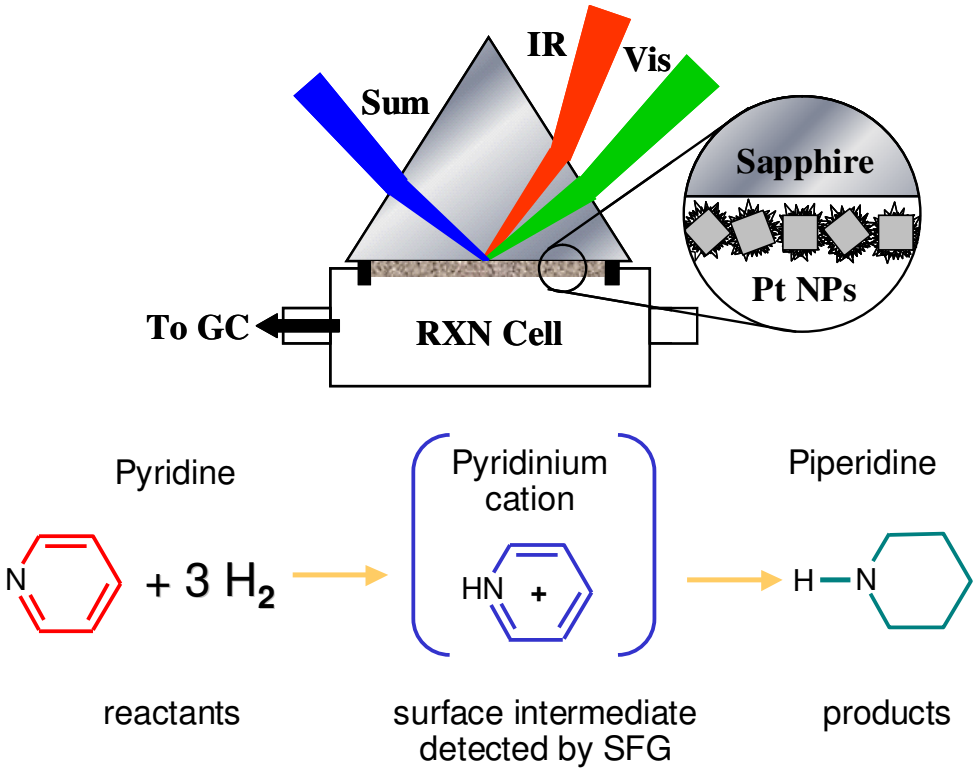
IR
Vis
Sum
Sapphire
Pt NPs
To GC
RXN Cell
Pyridine
Pyridinium cation
Piperidine
N
+ 3 H2
HN +
H N
reactants
surface intermediate detected by SFG
products

Figure 20.

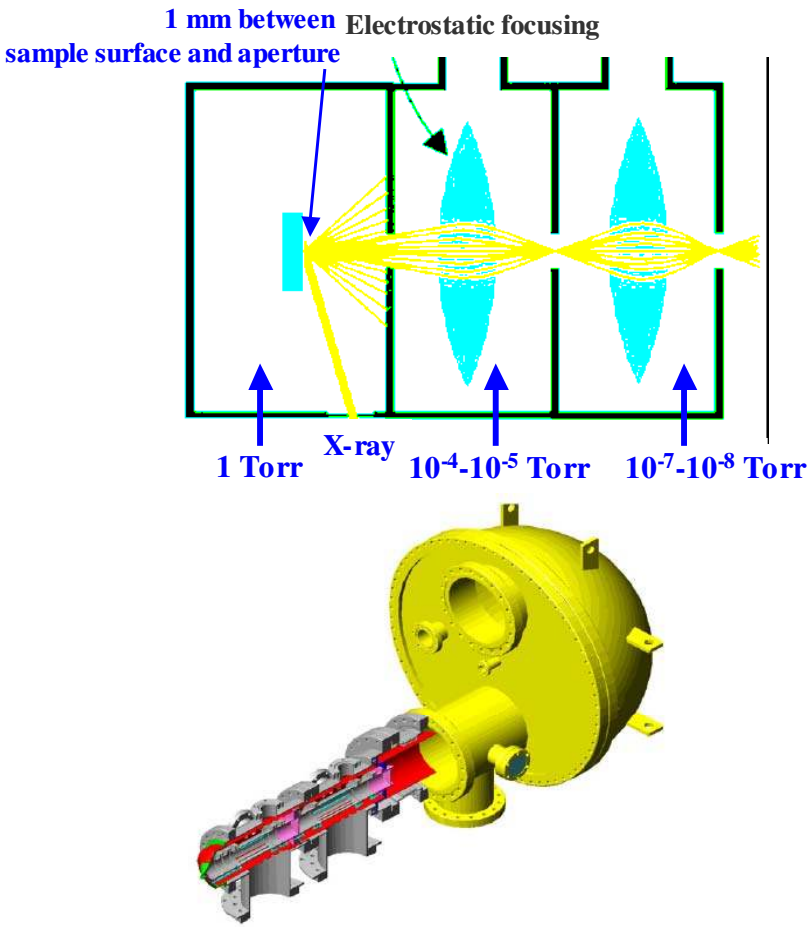
1 mm between
sample surface and aperture
Electrostatic focusing
1 Torr
X-ray
10-4-10-5 Torr
10-7-10-8 Torr

Figure 21.

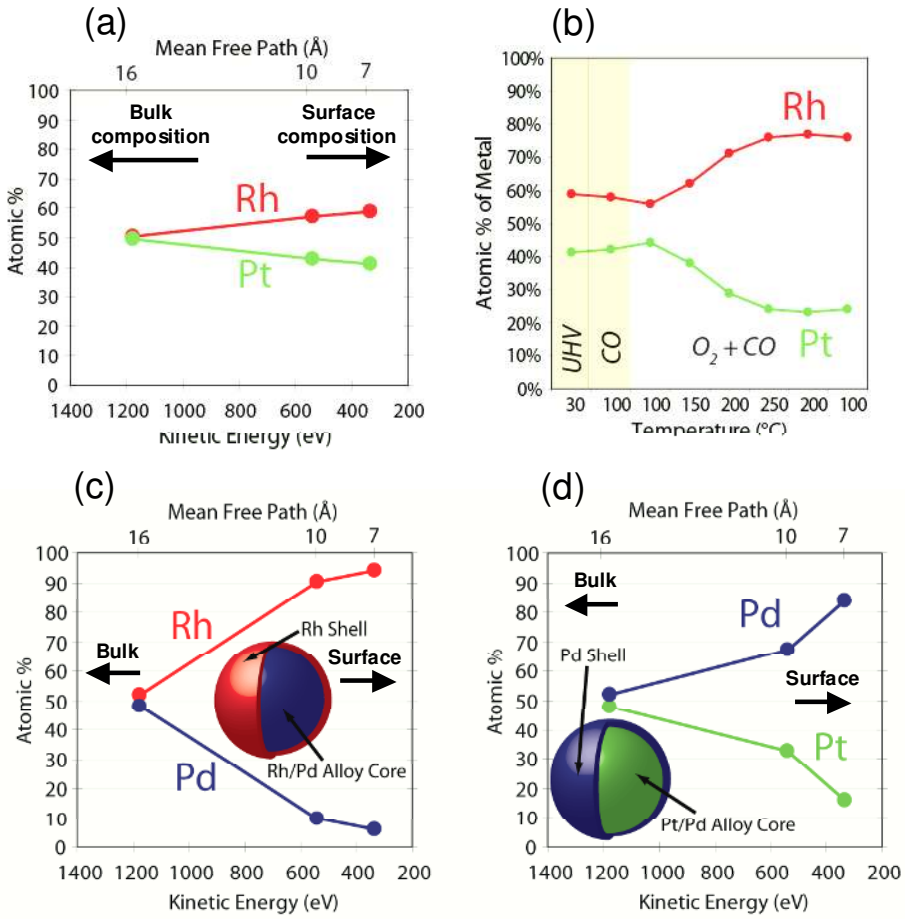
(a)
Mean Free Path (Å)
16
10
7
Bulk composition
Surface composition
Rh
Pt
Atomic %
Kinetic Energy (eV)
(b)
Atomic % of Metal
Rh
UHV
CO
O2 + CO
Pt
Temperature (°C)
(c)
Mean Free Path (Å)
Rh
Bulk
Rh Shell
Surface
Pd
Rh/Pd Alloy Core
Atomic %
Kinetic Energy (eV)
(d)
Mean Free Path (Å)
Bulk
Pd
Pd Shell
Surface
Pt
Pt/Pd Alloy Core
Atomic %
Kinetic Energy (eV)

Figure 22.

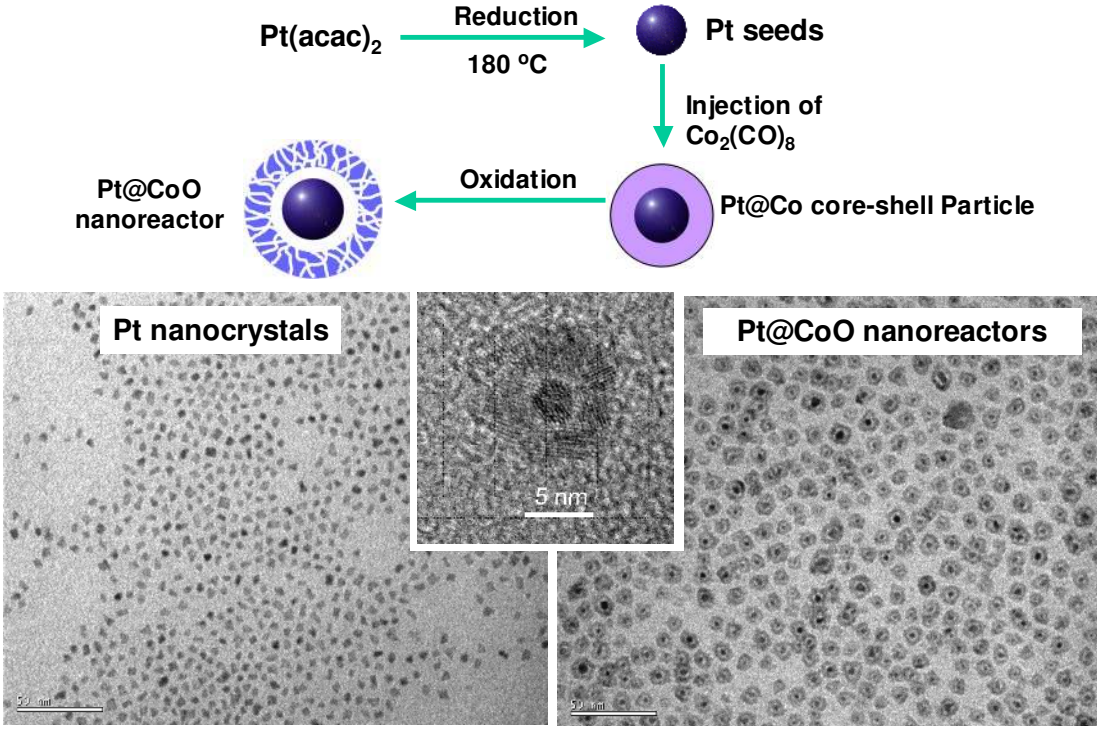
Pt(acac)2
Reduction
180 °C
Pt seeds
Injection of
Co2(CO)8
Pt@Co core-shell Particle
Oxidation
Pt@CoO
nanoreactor
Pt nanocrystals
5 nm
Pt@CoO nanoreactors

Figure 23.

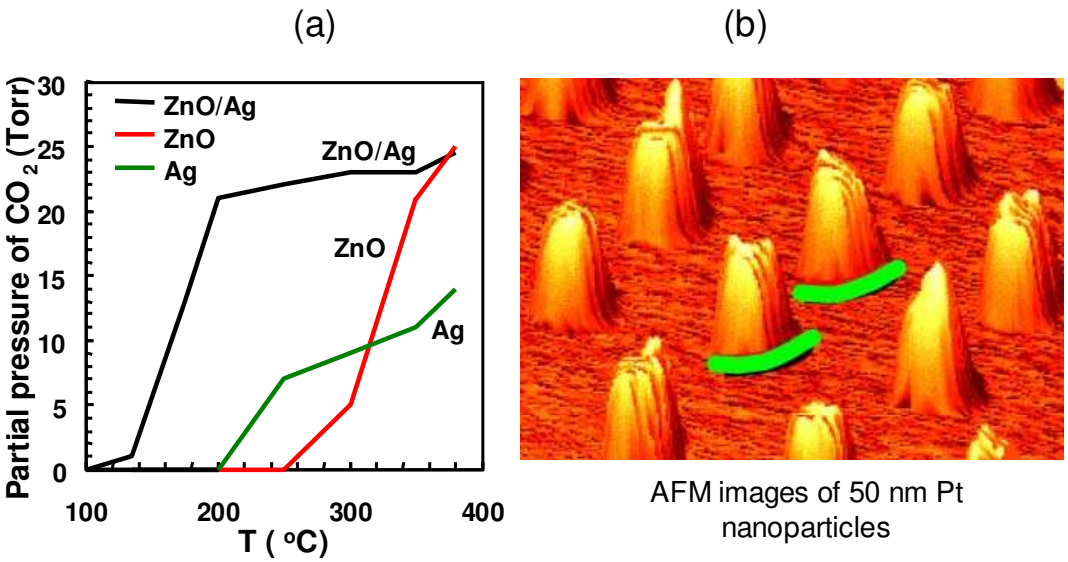
(a)
(b)
ZnO/Ag
ZnO
Ag
ZnO/Ag
ZnO
Ag
Partial pressure of CO_2 (Torr)
0
5
10
15
20
25
30
100
200
300
400
T (°C)
AFM images of 50 nm Pt nanoparticles

Figure 24.

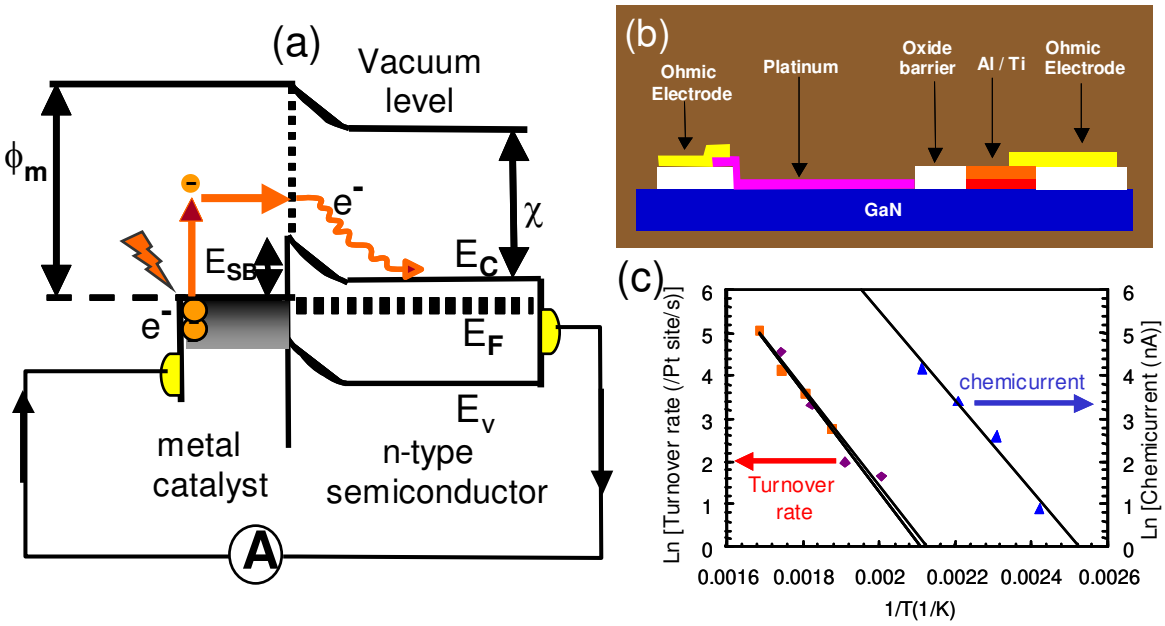
(a)
Vacuum level
ϕ_m
χ
E_{SB}
E_C
E_F
E_V
e-
e-
metal catalyst
n-type semiconductor
A
(b)
Ohmic Electrode
Platinum
Oxide barrier
Al / Ti
Ohmic Electrode
GaN
(c)
Ln [Turnover rate (/Pt site/s)]
Ln [Chemicurrent (nA)]
chemicurrent
Turnover rate
1/T(1/K)
0.0016
0.0018
0.002
0.0022
0.0024
0.0026

Figure 25.

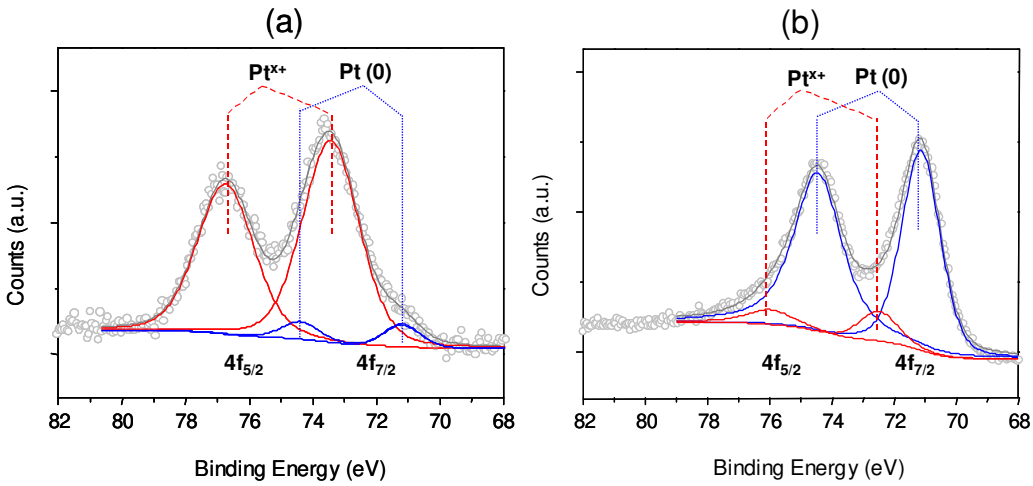
(a)
(b)
Pt^x+
Pt (0)
4f5/2
4f7/2
Counts (a.u.)
Binding Energy (eV)
82
80
78
76
74
72
70
68

Figure 26.